Article

Developmental Cell

Glutathione accelerates the cell cycle and cellular reprogramming in plant regeneration

Graphical abstract

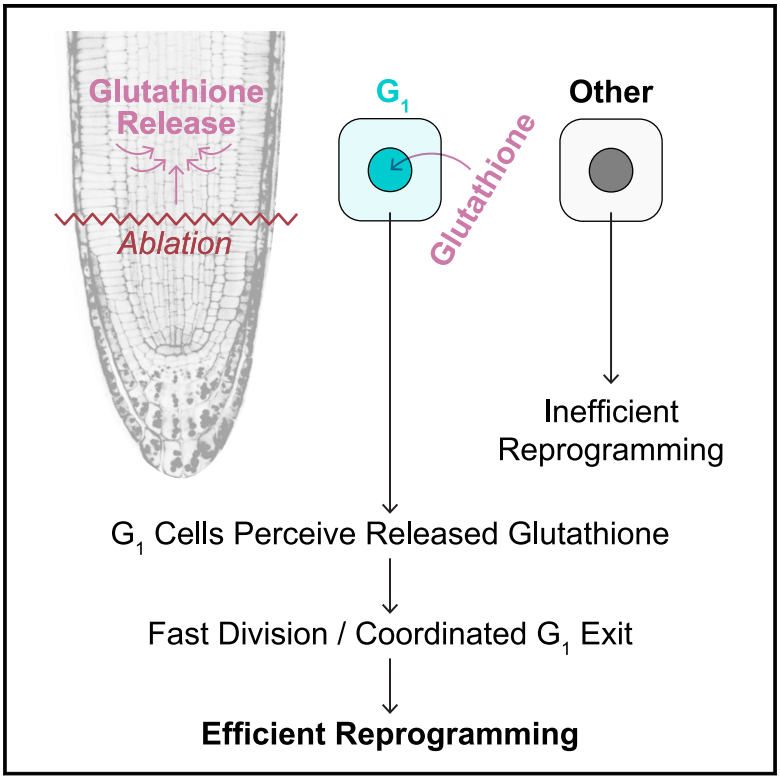

Authors

Laura R. Lee, Bruno Guillotin, Ramin Rahni, Chanel Hutchison, Bénédicte Desvoyes, Crisanto Gutierrez, Kenneth D. Birnbaum

Correspondence

ken.birnbaum@nyu.edu

In brief

In this study, Lee et al. demonstrate how a metabolite released by tissue damage, glutathione, instructs cells to embark on the first step of regeneration. Glutathione activates fast cell cycles in damaged plant organs, leading cells to rapidly change their identity to restructure a new organ.

Highlights

- Fast cell divisions during organ regeneration are driven by a shortened G1 phase
- Short G1 phases are correlated with efficient cellular reprogramming
- Glutathione during root injury coordinates short G1 phases across the organ
- Tissue-specific glutathione production regulates root growth and regeneration

Lee et al., 2025, Developmental Cell *60*, 1153–1167
April 21, 2025
https://doi.org/10.1016/j.devcel.2024.12.019

CellPress

Developmental Cell

CellPress

Article

Glutathione accelerates the cell cycle and cellular reprogramming in plant regeneration

Laura R. Lee,[1] Bruno Guillotin,[1] Ramin Rahni,[1] Chanel Hutchison,[1] Bénédicte Desvoyes,[2] Crisanto Gutierrez,[2] and Kenneth D. Birnbaum[1,3,*]

[1]New York University, Center for Genomics and Systems Biology, Department of Biology, New York, NY 10003, USA
[2]Centro de Biologia Molecular Severo Ochoa, 28049 Madrid, Spain
[3]Lead contact
*Correspondence: ken.birnbaum@nyu.edu
https://doi.org/10.1016/j.devcel.2024.12.019

SUMMARY

The plasticity of plant cells underlies their wide capacity to regenerate, with increasing evidence in plants and animals implicating cell-cycle dynamics in cellular reprogramming. To investigate the cell cycle during cellular reprogramming, we developed a comprehensive set of cell-cycle-phase markers in the Arabidopsis root. Using single-cell RNA sequencing profiles and live imaging during regeneration, we found that a subset of cells near an ablation injury dramatically increases division rate by truncating G1 phase. Cells in G1 undergo a transient nuclear peak of glutathione (GSH) prior to coordinated entry into S phase, followed by rapid divisions and cellular reprogramming. A symplastic block of the ground tissue impairs regeneration, which is rescued by exogenous GSH. We propose a model in which GSH from the outer tissues is released upon injury, licensing an exit from G1 near the wound to induce rapid cell division and reprogramming.

INTRODUCTION

Plants have remarkable regenerative capacity, where even a single somatic cell can give rise to an entire organism.[1] The *Arabidopsis* root apical meristem (RAM) provides a model for plant regeneration because the organ can regenerate from differentiated cells without exogenous hormones.[2] This process requires the coordination of both division and identity changes among the cells that will give rise to the regenerated tissue. How cell division properties are coordinated with cell-fate change in regeneration remains an open question.

Prior work in plants demonstrated links between cell-cycle control and cell-fate specification. In the *Arabidopsis* sepal, giant cells are specified when *Arabidopsis thaliana MERISTEM LAYER 1* (*ATML1*) expression exceeds a threshold level during G2/M phase.[3] Recent work showed that high protein levels of the cell-fate regulators SHORT ROOT (SHR) and SCARECROW (SCR) at a specific cell-cycle phase determine the polarity of a formative division in the root.[4] In the stomatal lineage, asymmetric and symmetric cell divisions are mediated by the expression of a series of master regulator basic helix-loop-helix (bHLH) transcription factors that concomitantly control cell identity (reviewed in Lee and Bergmann[5]).

After specification, cell-cycle length frequently changes as cells differentiate. For example, in the root meristem, cells divide faster along the maturation gradient as they move away from the stem cell niche,[6] largely due to a shortening of G1 duration.[7] Alternatively, in the stomatal lineage, G1 duration increases and cell cycles lengthen as cells terminally differentiate.[8] These observations suggest that even the trends of cell-cycle length dynamics during differentiation can differ between tissues. In the context of regeneration, cell division is required for complete repair of injured tissues.[2] There is considerable evidence in animals that events during G1 phase are critical for cell-fate establishment,[9–11] and short G1 phases are a known feature of totipotent animal stem cells.[12] It is not known in plants if rapid divisions facilitate organ formation or cell-fate specification in any of these contexts, including regeneration.

Different specialized plant cells can also show differences in their core cell-cycle machinery. While many cell-cycle regulators are conserved between plants and animals,[13,14] the expansion of cell-cycle gene families in plants has allowed for cellular specialization.[15] For instance, *CYCLIN D6;1* (*CYCD6*) is specifically expressed downstream of the SHR-SCR module and mediates a formative division that produces a new cell type.[16] *CYCLIN D7;1* (*CYCD7*) expression is restricted to the guard mother cell in the stomatal lineage and controls a switch from asymmetric to symmetric divisions.[17] This process is also controlled by another specialized cyclin, *CYCLIN D5;1* (*CYCD5*).[18]

These examples suggest that cell-type-specific control of the cell cycle in plants could be a more general phenomenon. One challenge facing the field has been studying the cell cycle in a way that maintains developmental context. Early transcriptional studies of the cell cycle in *Arabidopsis* employed synchronization of cultured cells,[19,20] which provided valuable insight but could not provide cell-type-specific information.

Both plants and animals can vary division rates by controlling the passage through G1 and G2 checkpoints, often controlled by

metabolites,[13,21] which are underexplored regulators of plant development. Recent work showed that tricarboxylic acid cycle metabolites[22] and reactive oxygen species (ROS)[23] may control root growth and development. Availability of glutathione (GSH)—the primary antioxidant in the cell[24]—and ROS patterning[25] in plants were previously linked to root growth and cell-cycle control.[25–28] GSH may be necessary for plant cells to pass the G1 to S transition,[26] and nuclear ROS levels change cyclically in cell-cycle-synchronized root tips.[29] Finally, evidence from Arabidopsis tissue culture suggests that GSH is transported into the nucleus in a cell-cycle-dependent manner.[27] While both GSH availability and cell-cycle control are linked to cellular reprogramming following injury, how these factors are coordinated during regeneration, if at all, remains unknown.

Here, we generate transcriptomic profiles of the cell cycle in the RAM while maintaining developmental context using single-cell RNA sequencing (scRNA-seq) and phase-sorted bulk RNA-seq, corroborating new phase markers with *in situ* hybridization. We used these data to establish a set of markers to analyze each phase of the cell cycle both broadly and among specific cell types. Collective analysis of these datasets identifies (1) many individual cell types have distinct cell-cycle dynamics at the transcriptional level and (2) G1 phase is uniquely tuned to respond to redox stress. During regeneration, we used both single-cell analysis and live imaging to show a dramatic shortening of G1 phase in cells near the injury. Furthermore, cells with a short G1-phase reprogram to new cell fates more rapidly than neighboring cells that maintain a longer G1. We demonstrate that GSH mediates both the rapid exit from G1 and fast divisions that preferentially lead to cellular reprogramming. Finally, the results showed that the middle and outer cell types appear to be a major source of GSH in the root that facilitates growth and regeneration. Overall, we show that GSH acts as a signal in regeneration where, upon wounding, GSH enters the nucleus, prompting a rapid exit from G1, a fast cell cycle, and cell-fate reprogramming. Our work establishes a role for GSH as an injury communication signal that controls cell-cycle duration to mediate organ regeneration.

RESULTS

Phase-enriched scRNA-seq libraries identify a large set of cell-cycle-controlled genes

To gain a deeper view of cell-cycle dynamics in specific cell types, we sought to characterize cell-cycle transcriptomes in intact Arabidopsis roots while maintaining developmental context. We synchronized cells *in vivo* using hydroxyurea (HU)[30] followed by scRNA-seq to obtain phase-enriched populations in which cell-type-specific information is maintained (Figures 1A, 1B, S1, and S2). We performed a differential expression analysis to identify phase marker genes (Figures S3A–S3C) that we corroborated with bulk RNA-seq profiles from cells sorted by ploidy using fluorescence-activated cell sorting (FACS) as a proxy for phase (Figure S4A and S4B).

We then used the stringent top-50 marker set (Table S1) to assign our synchronized cells to phases in Seurat[31] (Figure 1B) and examined the expression of known G2- and S-phase marker genes with functional roles in the cell cycle (Figure 1C; Table S2). Canonical G2/M markers—cyclin Bs—and the S-phase markers—minichromosome maintenance complex (MCM)—were classified to the appropriate phase. The origin recognition complex (ORC) family, which is required in S-phase to license DNA replication, appeared to be expressed more highly in G1. This is consistent with the observation that ORCs are required in the pre-replication complex prior to MCMs (reviewed in Fragkos et al.[32]) and supports that this set of phase markers provides a sensitive discrimination between G1 and S phase.

To validate these markers *in vivo*, we visualized transcripts directly using multicolor *in situ* hybridization (Figures 1D and S3D–S3G). We observed a novel G2/M marker—AT4G23800—co-staining with a probe for the well-known G2/M marker CYCB1;1. Additionally, both markers were present in cells with mitotic figures, visualized with DAPI, further confirming the novel marker is expressed in cells in G2/M phase.

To validate a G1 probe, we co-stained a putative G1 marker—AT5G21940—with a well-established S marker—AT5G10390 (H3.1).[33] In this case, we tested for anticorrelation of these markers and exclusion from mitotic figures because there are no known G1 transcriptional markers in plants. As predicted, we found these two transcripts were anticorrelated and absent from mitotic figures, with occasional overlap (Figures 1D and S3D–S3G). Thus, the marker set provides a highly sensitive tool for cell-cycle analysis in single-cell studies and, importantly, a method to distinguish cells in G1 phase, allowing enhanced analysis of the role of G1 in plants.

As expected, Gene Ontology (GO) enrichment analysis found that cell-cycle-related terms were enriched in G2/M and S phases (Figure 1E; Table S3). However, we found that canonical cell-cycle markers are correctly but lowly expressed (Figures S4C and S4D) so the most robust markers did not include cyclins (Figure S4E). Notably, many markers were enriched in, but not necessarily specific to, any given phase, showing that, beyond the distinct transcriptome of G2/M, other phases had less discrete transitions at the transcriptional level.

Interestingly, the top 50 G1 markers were enriched for GO terms related to oxidative stress (Figure 1E; Table S3). This enrichment of ontology terms in G1 cells was also present in the G1 ploidy-sorted dataset, which ruled out a batch effect (Table S3). This suggests a role for oxidative stress management within G1. Overall, the dataset now provides a robust tool to analyze the cell cycle in single-cell profiles and identifies genes with potential roles in specific cell-cycle phases.

Pseudotime analysis identifies cell-cycle variation within and between cell types

We sought to generate a fine-grained analysis of cell-type-specific cell-cycle patterns in the Arabidopsis root. Using a scRNA-seq profile of all cells in the root meristem,[34] cells were aligned in cell-cycle pseudotime (Figure 2A). The trajectories proceed from G2/M and to G1, where they split into three separate branches that each continue to S phase. Different cell types favored—but were not restricted to—distinct regions of the uniform manifold approximation and projection (UMAP) space (Figures 2B and S5). Thus, cells clustered by their *in vivo* identity using only stringent cell-cycle markers, suggesting the separate branches for one cell-cycle phase represented cell-type-specific cell cycles.

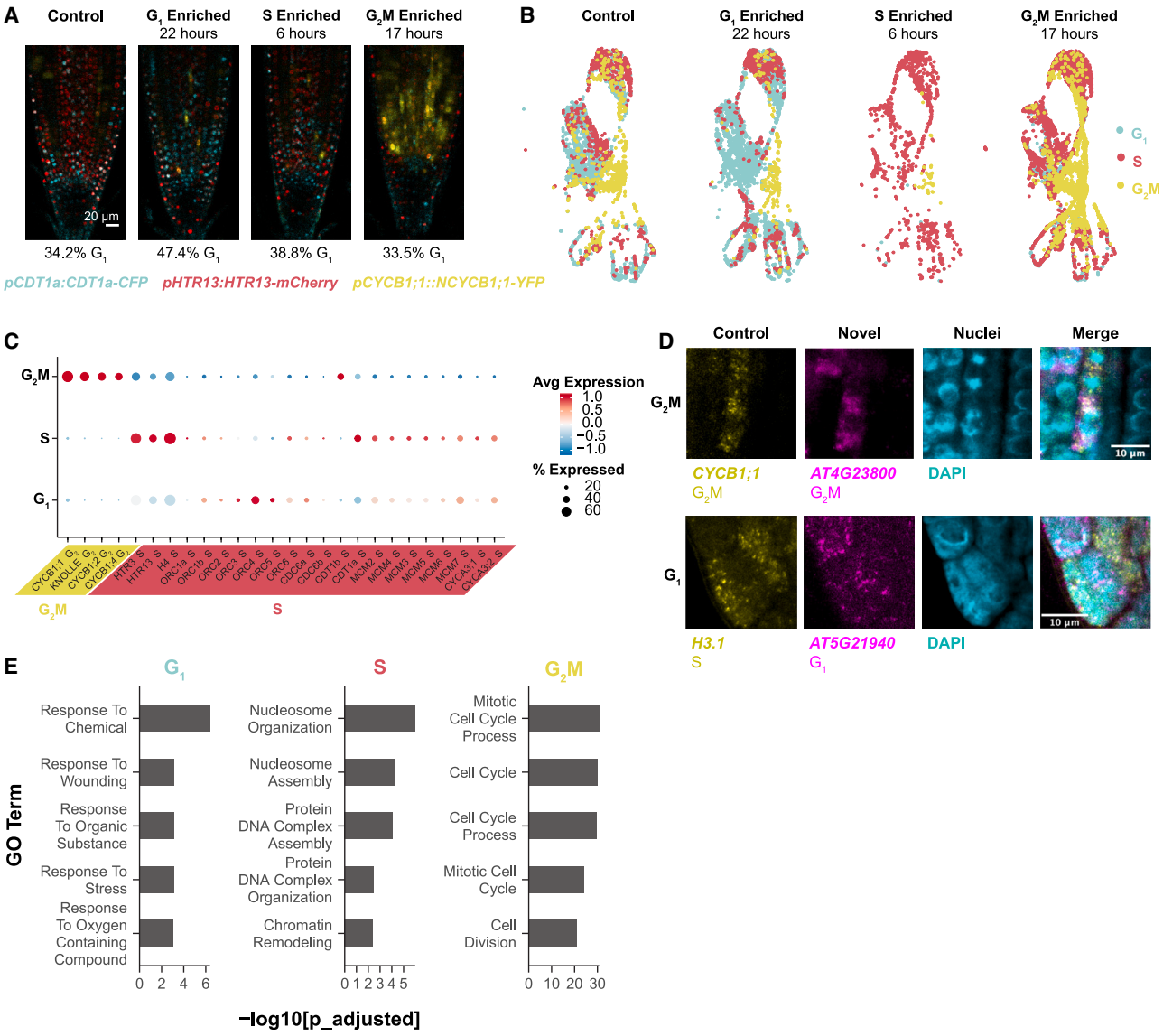

Figure 1. Single-cell phase-synchronized cells yield robust transcriptional markers for each phase of the cell cycle

(A) Representative images of phase enrichments achieved with HU synchronization using seedlings expressing the PlaCCI reporter. The G1 reporter *pCDT1a:CDT1a-CFP* is shown in cyan, the S reporter *pHTR13:HTR13-mCherry* is shown in red, and the G2/M reporter *pCYCB1;1:NCYCB1;1-YFP* is shown in yellow. The percentage of cells in G1 (CFP-positive cells/all cells), determined from 3D segmentation of z stacks, is shown below each panel. Scale bar = 20 μm.

(B) An unsynchronized control and three single-cell profiles collected at specific times after synchronization (enriched for different cell-cycle phases) integrated in UMAP with cells color coded by phase determination. Cells from each time point were separated after integration.

(C) A dot plot showing expression of gold standard cell-cycle-phase markers, showing known G2/M-phase markers followed by known S-phase markers.

(D) *In situ* hybridization of novel G1 and G2/M probes. Known markers are shown in yellow and new markers in magenta. The new G2/M marker is hybridized alongside a known G2/M marker, showing overlap. The new G1 marker is hybridized alongside a known S marker, showing spatial anticorrelation. Scale bar = 10 μm.

(E) The top five most statistically significantly enriched GO terms among the top 50 phase marker set for each phase.

See also Figures S1–S4 and Tables S1, S2, and S3.

The most apparent trend was a difference in G1 to S branches between inner and outer cell types. Xylem and phloem occupied successive layers of a left branch, with endodermis and cortex on an outermost layer of that branch (Figure 2B). Epidermal cell types occupied a distinct second branch, and a third branch contained the slow-cycling cells around the quiescent center (QC), the core of the stem cell niche (Figure 2B). This distinct stem cell behavior is in accordance with the well-documented slower rate of division of these cells compared with the more proximally located (shootward) transit-amplifying cells.[6,7,35] The epidermal G1 branch was enriched for genes related to translation, while the stele-endodermis-cortex G1 branch was characterized by gene expression related to cell-wall synthesis (Figure 2C; Table S4). This suggests that the specialized

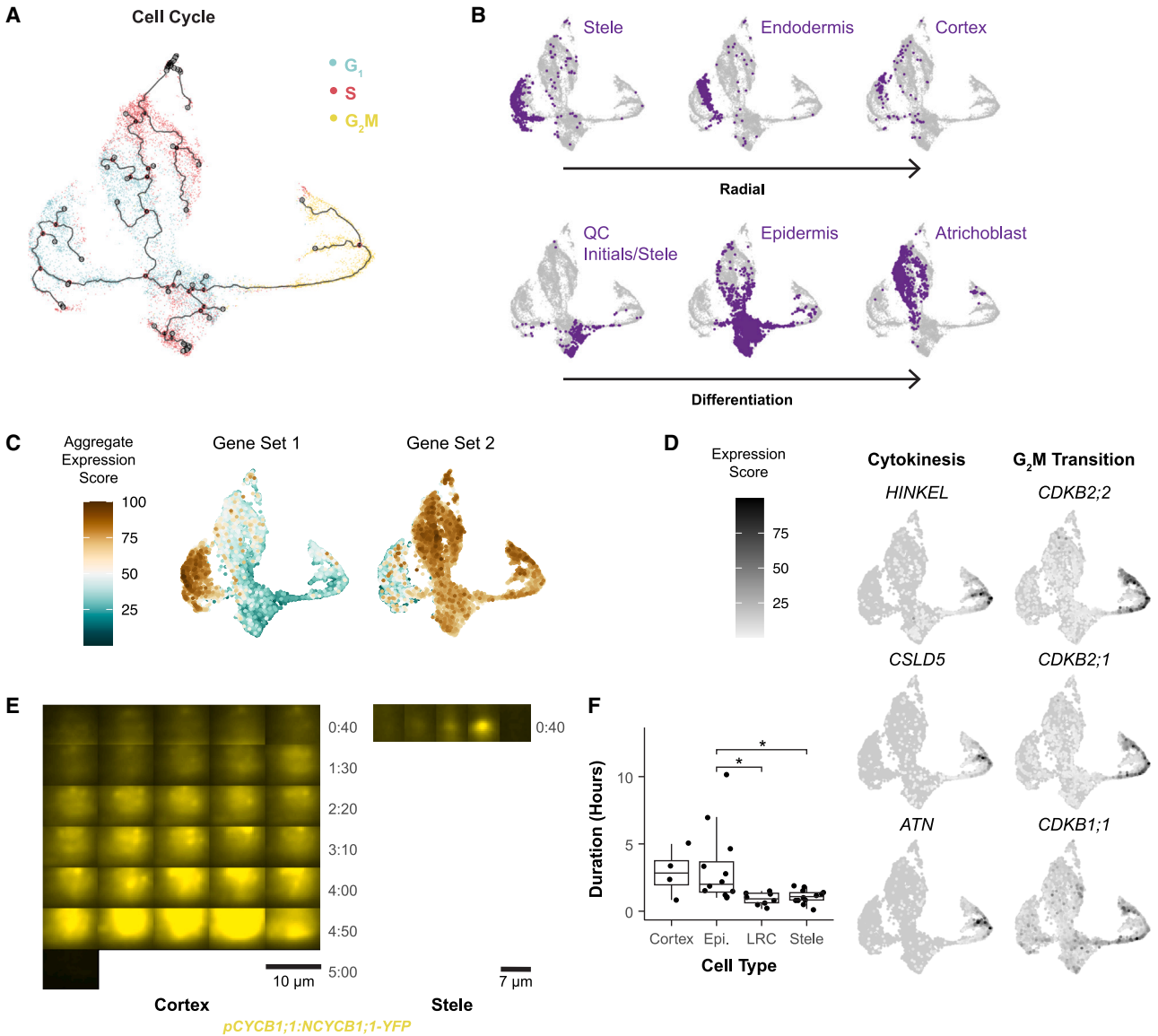

Figure 2. Different cell types follow different trajectories through the cell cycle

(A) Pseudotime map of cells clustered using only cell-cycle markers and colored by phase assigned in Seurat.

(B) In the same UMAP clustering in (A), cells were labeled by their independently determined cell identity, showing groupings by both developmental stage and radial cell identity. Arrows indicate inner to outer cell files (top) and differentiation stage from young to older (bottom).

(C) Aggregate expression of genes enriched in either the epidermal or stele-endodermis-cortex G1 branch.

(D) UMAPs showing gene expression specific to sub-regions of the G2/M branch, with representative genes involved in cytokinesis (lower branch) and the G2/M transition (upper branch).

(E) Variable lengths of G2/M marker expression shown between one cortex and one stele cell. Each frame is 10 min apart from time-lapse movies taken with a Tilt light sheet system (Mizar). Each montage shows the frame at which *pCYCB1;1:NCYCB1;1-YFP* first becomes visible to the frame where the reporter disappears, indicating the end of G2/M. Scale bar = 10 µm.

(F) Quantification of G2/M duration based on the amount of time *pCYCB1;1:NCYCB1;1-YFP* was visible for in cells from two time-lapses ($n = 36$ cells). Asterisks represent significant differences in G2/M duration ($p < 0.05$, pairwise t test). Each dot represents a cell.

See also Figure S5 and Table S3 and Video S1.

functions of specific cell types are at least partially controlled within the cell cycle as they mature in the meristem. The overall patterns were consistent with the hypothesis that plant cells have multiple G1 modes.[36] As a resource, we generated a list of markers that were specific to cell types and differentially expressed by phase (Table S6).

In addition, while many genes were commonly expressed across G2/M cells, we observed a distinct upper branch of G2/M cells that expressed genes that control the G2/M transition and a lower branch of G2/M cells expressing cytokinesis regulators (Figures 2A and 2D). We also observed differences in the number of cells in the G2/M branch among different cell types

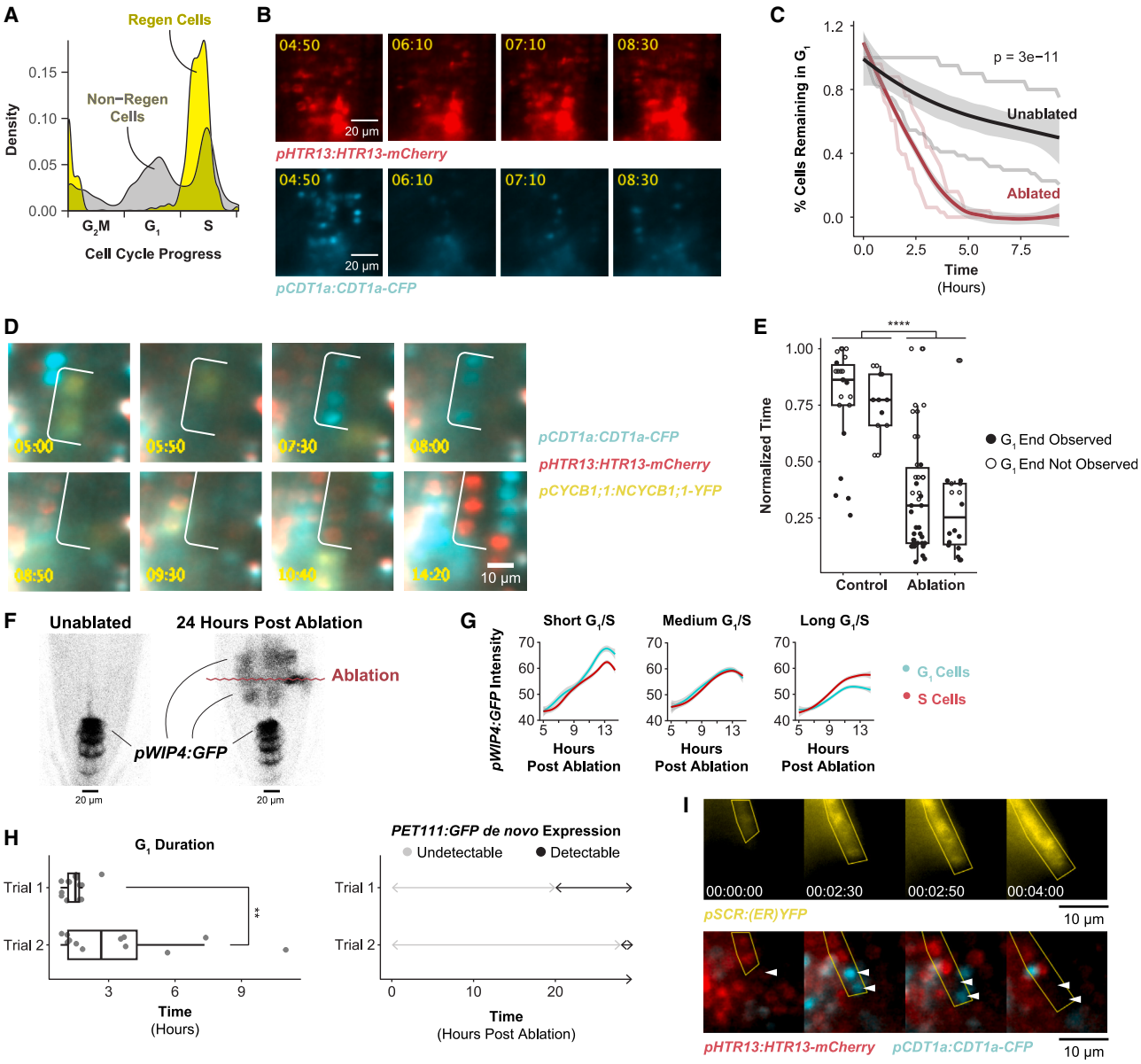

Figure 3. The G1 phase of the cell cycle is dramatically truncated in regenerating cells

(A) Summary of the frequency of a given cell-cycle phase in regenerating (yellow) and non-regenerating (gray) cells. Cells are aligned along a cell-cycle pseudotime on the x axis, with their density shown on the y axis.

(B) Representative images of cells coordinately exiting G1 following tissue damage (bottom). S-phase cells (top) serve as a control showing a continuous strong signal (no depletion) in the same roots. Time is shown in h:min, and 00:00 is the time of the ablation. Scale bar = 20 μm.

(C) Quantification of the coordinated G1 exit shown as a survival analysis of the population of G1 cells identified at the beginning of the time-lapse. The y axis represents the fraction of G1 cells from time zero (the first frame of the time-lapse) still in G1 at time n. The x axis shows time since the beginning of the time-lapse. Time zero for each ablated root is 3 hpa. Two unablated and two ablated roots were analyzed (n = 165 cells, p value = 3e−11, log-rank test).

(D) Representative time-lapse series of a short G1 in an ablated root. Scale bar = 10 μm.

(E) Quantification of G1 duration in control and ablated roots for two trials. Filled dots represent cells in which the end of G1 was observed. (n = 94 cells, p value = 3.221e−09, Mann-Whitney U test.)

(F) Representative image of the *pWIP4:GFP* expression domain before ablation and 24 hpa. Scale bar = 20 μm.

(G) Quantification of *pWIP4:GFP* signal over time in G1- and S-phase cells, with different plots showing analysis of cells grouped by the length of G1 or S. Bins are defined as short <3 h, medium >3 and <6 h, long >6 and <9 h. (n = 650 cells in 1 root).

(H) Quantification of G1 duration in two roots (left) and the timing of *PET111* expression establishment in the regeneration zone in the same two roots (right) showing the association between G1 duration and *PET111* appearance. Trials refer to individual root time-lapses (p value = 0.00413 Mann-Whitney test).

(legend continued on next page)

(Figure S5D). We reasoned this could indicate differences in the amount of time cells spent in a given sub-phase of G2/M. To test this hypothesis *in vivo*, we generated long-term time-lapse light sheet microscopy movies of roots expressing the three-color cell-cycle translational reporter, PlaCCI (plant cell cycle indicator), which marks G1 (CDT1a, cyan), S (HTR13, red), and late G2 through M phase (CYCB1;1, yellow[37]). We measured G2/M duration in epidermal, cortical, stele, and lateral root cap cells (Figures 2E and 2F; Video S1). Epidermal and cortical cells remained in G2/M twice as long as stele and lateral root cap cells. But there was also significant variation in G2/M duration within cell types (Figure 2F). Thus, live imaging corroborated the cell-type-specific phase-dwelling variations detected by the cell-cycle mapping of scRNA-seq profiles. Overall, these observations identify the extent to which the cell cycle is tailored to cell identity and developmental stage.

Tissue-wide coordinated G1 exit and rapid G1 is linked to regeneration efficiency

Many questions in plant and animal regeneration concern how cell-cycle control mediates cellular reprogramming. For example, we have observed that cell-cycle speed increases during RAM regeneration,[34] but it remains unclear whether this is due to a uniform increase in speed across cell-cycle phases or whether certain phases are truncated to achieve fast divisions. Thus, we applied the cell-cycle marker analysis to scRNA-seq profiles of regenerating cells following root tip excision over a time course of 4 to 36 h post-cut[34] (hpc) to analyze changing cell-cycle dynamics between regenerating and non-regenerating cells. Aligning these groups of cells in cell-cycle pseudotime showed that regenerating cells disproportionately accumulate at the G1 to S transition and are largely absent from G1 (Figure 3A).

This result suggests that G1 is dramatically shortened relative to the other cell-cycle phases during early regeneration. To measure G1 duration together with fate re-specification *in vivo*, we used time-lapse light sheet imaging on live regenerating roots, quantifying G1 duration concurrently with cell-fate changes using the cell-cycle marker, PlaCCI,[37] and a reporter for the QC-columella marker *WIP DOMAIN PROTEIN 4 (WIP4)*, *pWIP4:GFP*.[38] WIP4 marker expression shootward of the ablation marks cells that are in the process of reprogramming from stele to QC and columella fates in the newly formed meristem. By monitoring this region, we could track the full history of cell-cycle phases, their duration, and reprogramming state.

We observed that cells in the regeneration zone coordinately exited G1 approximately 6 h post-ablation (hpa), within 1 to 2 h of one another, depending on biological replicate, and prior to new *pWIP4:GFP* expression (Figures 3B and 3C; Videos S2 and S3). We quantified whether this behavior differed from G1 cells in unablated roots with a G1 survival analysis to measure the timing of G1 exit in a population of cells. We observed a much more rapid decay in ablated roots compared with unablated roots (log-rank test p value = 3e−11)—consistent with the dramatic depletion of G1 cells detected in the scRNA-seq analysis (Figure 3A).

Following a coordinated G1 exit and between 8 to 12 hpa, these cells then proceeded through G1 at an accelerated rate (Figures 3D and 3E; Table S5). To quantify G1 length, we measured the elapsed time between when CDT1a became visible after mitosis (early G1) to when CDT1a was degraded, indicating S-phase entry, and found a statistically significant difference between control and ablated roots. Overall, the data show there are two associated phenomenon: (1) a coordinated exit from G1 (Figures 3B and 3C) and (2) a shortened G1 phase that dramatically speeds the rate of the cell cycle (Figures 3D and 3E).

To test the association between rapid G1 and reprogramming, we identified cells that eventually expressed the *pWIP4:GFP* marker (indicating cellular reprogramming, Figure 3F) and analyzed their cell-cycle dynamics retrospectively in time-lapse movies. We compared the timing of re-specification in cells with short G1s versus neighboring cells that displayed longer G1s (Figure 3G). The analysis showed that short G1 cells gained higher *WIP4* marker expression levels than nearby cells with long G1 (Figure 3G). There was no relationship between *WIP4* marker expression and G1 duration in unablated roots (Figure S6). Thus, cells in the regenerating meristem that undergo fast G1 reprogram more rapidly than slower G1 neighbors.

To determine whether the relationship between G1 length and re-specification holds for other markers that are expressed later during regeneration, we looked at an enhancer trap late-stage marker for columella, *PET111:YFP*. In this case, we exploited variability in *PET111:YFP* return time and G1 duration between roots to explore whether these two variables were correlated. In this analysis, G1 duration was also broadly predictive of PET111 re-appearance (Figure 3H).

We used the endodermal/QC marker *pSCR:erYFP* in the PlaCCI background to test the link between G1 and reprogramming in a radial cell file. New endodermal fate establishment is a rare event, but, across two time-lapses, we observed five cases of cells establishing *de novo SCR* expression. In each of the five cases, *de novo* expression was established in cells that were in a rapid G1 phase (Figure 3I). Thus, rapid G1s in plant root regeneration are tightly associated with reprogramming of cell fate. This opens the possibility that rapid G1 could play a functional role in promoting cellular reprogramming in plants.

GSH is enriched in G1 nuclei at steady state and immediately following tissue damage

Having implicated G1 duration in regeneration efficiency control, we next sought to establish a mechanistic link between injury and cell-cycle control. The finding above showing "response to wounding" and "response to oxygen-containing compound" terms enriched in G1 was intriguing because ROS has potential links to both the cell cycle and wounding[25,26,39,40] (Figure 1F). Thus, we reasoned that G1 cells could be primed to respond to ROS signals generated by tissue damage.

To explore this connection, we performed live imaging with the ROS indicator 2',7'-dichlorodihydrofluorescein diacetate (H2DCFDA) and the GSH dyes 7-amino-4- chloromethylcoumarin

(I) Representative image of the expansion of the expression domain of the *pSCR:erYFP* reporter during regeneration. The SCR expression domain is outlined with a yellow region of interest (ROI) on both the upper and lower panels. Panels were chosen to show a cell just before division, marked with an arrow. They then show the daughters go through G1. The timestamp of each frame is shown (day:h:min) starting at 26 hpa. Scale bar = 10 μm.
See also Figure S6 and Tables S4 and S5 and Videos S2 and S3.

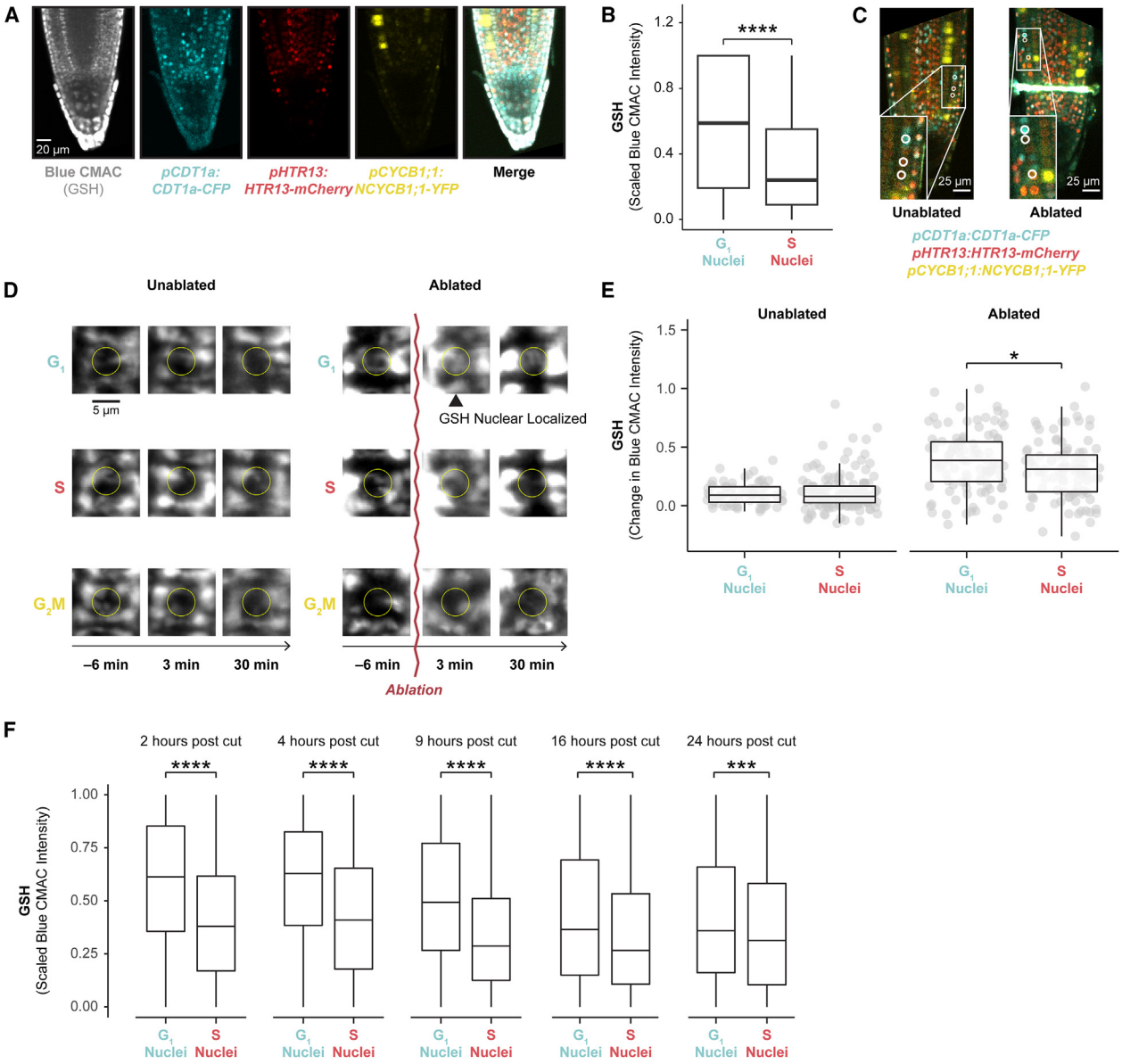

Figure 4. Regenerating cells import glutathione to the nucleus in G1

(A) Representative confocal microscopy image of a PlaCCI seedling stained with Blue CMAC overnight. Scale bar = 20 μm.

(B) Quantification of Blue CMAC in G1- and S-phase nuclei. n = 416 nuclei, n = 2 roots, p value = 2.23e−10, Student's t test.

(C) Images showing the location of cells analyzed in 4D shown in insets. Scale bar = 25 μm.

(D) Representative images of cells in each phase of the cell cycle in control and ablated roots shown in a time-series montage. Time relative to ablation is shown, with an arbitrary equivalent time span for unablated roots. The yellow circle shows the position of the nucleus. Scale bar = 5 μm.

(E) Quantification of the change in Blue CMAC levels following ablation relative to their level prior to ablation in nuclei of cells in G1 and S phase in unablated and ablated roots. Each boxplot shows GSH signal measured in segmented nuclei from frame 3 of the relevant time-lapse. In the ablated root, this frame was taken 3 min post-ablation (n = 420 nuclei and 2 roots, p value = 0.0296, Student's t test).

(F) GSH levels are shown in segmented nuclei at various time points post cut in G1- and S-phase cells (n = 8,632 nuclei, n = 35 roots, ***p < 5e−4, ****p < 7e−9, Student's t test).

See also Figures S6 and S7 and Video S4.

(Blue CMAC) and 5- chloromethylfluorescein diacetate (CMFDA) during stereotypical root growth and regeneration. We first confirmed that these dyes had no effect on meristem size and regeneration efficiency (Figures 4A, S6, and S7). We used time-lapse confocal imaging and the ablation described above to observe GSH localization within the first 30 min of tissue damage. We found that, in control roots, Blue CMAC signal was higher in G1-phase nuclei than in S-phase nuclei (Figure 4B), building on prior evidence that suggested nuclear GSH controls the G1 to S transition.[26,27] In regeneration, we observed a pulse of nuclear

GSH immediately after ablation within nuclei just above the injury site across all cell types (Figures 4C–4E; Video S4). In addition, at the 2- and 4-hpc time points in the root cutting injury, nuclei that showed the highest CMAC signal shootward of the cut site were in the same region in which cells undergo rapid G1 phases (Figure S7), with CMAC signal remaining high in G1 cells through 24 hpc (Figure 4F). Overall, the results suggested that the earliest cells to reprogram first undergo a local burst of GSH import into the nucleus then a coordinated G1 exit followed by a rapid G1 phase.

GSH depletion inhibits regeneration efficiency

To explore the functional role of GSH in regeneration, we depleted GSH during regeneration using the GSH synthesis inhibitor, L-buthionine-sulfoximine (BSO), following established protocols[28] and then tested for regeneration defects. BSO inhibits GLUTAMATE-CYSTEINE LIGASE (GSH1), which encodes the rate-limiting step of GSH formation.[41] While roots treated with 1 mM BSO exhibited a strong depletion of GSH and regeneration defects as observed by the *pWIP4:GFP* cell identity marker (Figures 5A and 5B), these plants also showed stunted growth before ablation (as previously observed[28]), raising the possibility that pre-injury meristem defects impaired regeneration. To address this issue, roots were germinated on a lower concentration of BSO (0.5 mM) on which they displayed normal morphology.[28] Although ablated roots grown on 0.5 mM BSO eventually regenerated, they showed a lower amount of *pWIP4:GFP* expression in the regeneration zone at 24 hpa (Figures 5C and 5D). Thus, depletion of GSH to a level that does not affect stereotypical root growth still impairs the respecification of the columella and QC marker.

To quantitatively assess the effect of GSH depletion on regeneration efficiency, we monitored the number of cells containing amyloplasts—a physical marker for columella identity, which is necessary for gravity response—in excised root tips with modified pseudo Schiff-propidium iodide (mPS-PI) staining[42] at 18 hpc. We found that treatment with BSO significantly decreased the number of cells with *de novo* amyloplast formation at 18 hpc and that co-treatment with GSH rescued amyloplast formation to the level of untreated roots (Figures 5E and 5F), consistent with regeneration defects caused by diminished levels of GSH post-injury. Finally, to confirm that BSO inhibits regeneration specifically by depleting GSH, we performed gravitropism experiments with an Arabidopsis line harboring a mutant allele of GSH1,[26] *cadmium sensitive2* (*cad2-1*),[43] on increasing BSO concentrations (Figure 5G). This mutant line has a point mutation in the domain where BSO physically interacts with GSH1,[43] rendering the mutant insensitive to BSO treatment. At 0.25 and 0.375 mM BSO, *cad2-1* roots regenerated more efficiently than wild type, confirming BSO's specific effect on GSH in this context and the role of GSH biosynthesis in regeneration.

We next directly tested whether BSO treatment perturbs G1 dynamics during regeneration by performing long-term time-lapse imaging in PlaCCI roots germinated on 0.5 mM BSO. Following injury, G1 cells in BSO-treated roots failed to undergo the coordinated exit that we observed in untreated roots (Figure 6A). Using a survival analysis of G1 cells again, we found that the time cells remained in G1 was significantly prolonged in BSO-treated roots (Figure 6B, log-rank test; p value $< 2e{-}16$).

Interestingly, BSO appeared to have a greater effect on cells away from the immediate injury site. In BSO-treated roots, most cells above the injury failed to undergo coordinated G1 exit, while the first two or so layers of cells near the cut site still showed coordinated exit despite BSO treatment (Figure 6C). This is consistent with a gradient of GSH that is highest in cells immediately adjacent to the wound site dissipating in more proximal cells, where BSO was presumably more competent to disrupt GSH signaling.

Overall, the effects of the BSO treatment on *pWIP4:GFP* expression levels (Figures 5C and 5D), amyloplast formation (Figures 5E and 5F), and G1 dynamics (Figure 6) lead to the conclusion that GSH depletion slows regeneration at least in part through modifying G1 exit and duration.

Ground tissue is an apparent source of GSH in growth and regeneration

In our staining for GSH in unablated roots, we observed a striking pattern in which Blue CMAC was highly localized to the cap, epidermis, and ground tissue (cortex and endodermis), while the stele stained much more weakly (Figure 4A, leftmost panel). The pattern did not appear to be an artifact of limited cell penetration, as the two GSH dyes, Blue CMAC and CMFDA, have similar staining patterns, while the ROS indicator, H2DCFDA, which has a similar chemical structure to CMFDA,[44] stains all files relatively evenly (Figure S6C). In particular, both Blue CMAC and CMFDA showed highly concentrated staining in the endodermis and cortex (Figure S6C). The localization pattern was consistent with independent data we gathered from scRNA-seq profiles showing GSH biosynthesis genes are also highly expressed in the ground tissue (Figure S6D). Therefore, we hypothesized that ground tissue could be a source of GSH for root growth and rapid dissemination upon injury.

Metabolites and other small molecules can travel rapidly between plant cells through symplastic connections that form tunnels between adjacent cell walls called plasmodesmata.[45] To ask whether ground tissue serves as a source of GSH for other files to enable homeostatic growth and regeneration, we employed a callose-synthase induction system that blocks symplastic transport out of the ground tissue[46] and then assayed for growth and regeneration efficiency (Figures 7A and 7B). Exogenous GSH is known to enhance growth rates in Arabidopsis roots, so we controlled for the nonspecific effects on growth by comparison to high sucrose (1% versus the standard 0.5%), which also enhances root growth. Accordingly, sucrose and GSH both increased growth rates in control roots. However, only GSH-treated roots partially rescued the growth of the ground-tissue-blocked roots (Figure 7A). Furthermore, after injury and a symplastic block of ground tissue, GSH, but not sucrose, rescued regeneration efficiency (Figure 7B). Finally, we confirmed that induction of callose synthase in the ground tissue resulted in depleted GSH in the stele by staining-induced roots with Blue CMAC (Figure 7C, $n = 21$ roots, p value $= 0.0041$). The results suggest that ground tissue is a source of GSH for normal growth and tissue regeneration, mediating a rapid exit from G1, an abbreviated cell cycle, and rapid cellular reprogramming in the neighboring stele cells.

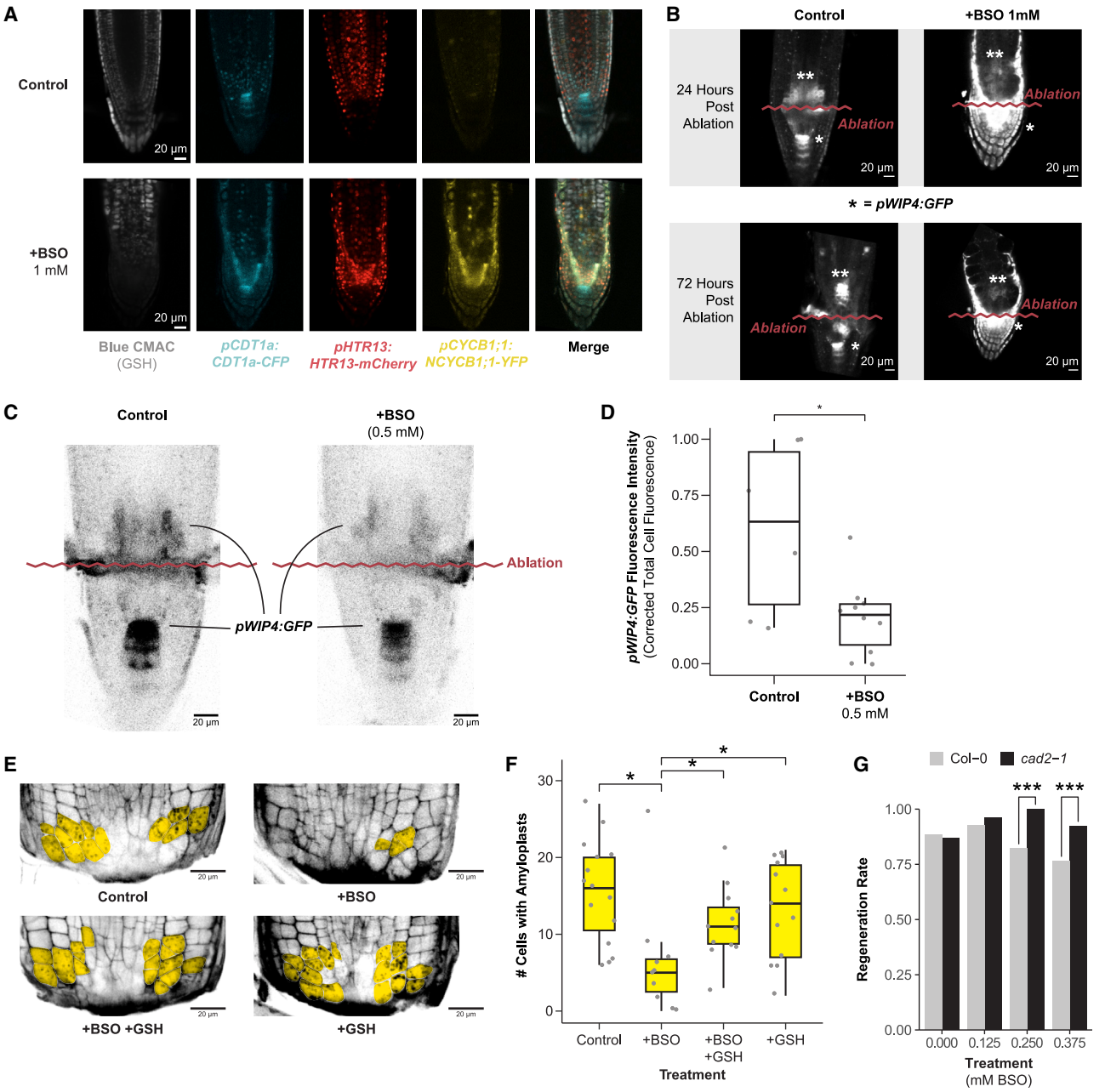

Figure 5. Depletion of GSH biosynthesis with BSO impairs regeneration and is rescued by exogenous GSH

(A) 7-day-post-germination (dpg) root meristems (PlaCCI × *pWIP4:GFP*) grown on MS (control) or on MS + 1 mM BSO then stained overnight with Blue CMAC. Scale bar = 20 μm.

(B) Representative images of the *pWIP4:GFP* signal in a median section of a control and BSO-treated root at 24 and 72 HPA. The original QC within the stem cell niche is indicated with an asterisk (*), and the newly forming stem cell niche is marked with two asterisks (**). Scale bar = 20 μm.

(C) Representative images of *pWIP4:GFP* signal 24 hpa in control and 0.5 mM BSO treatment. Scale bar = 20 μm.

(D) Quantification of *pWIP4:GFP* signal in the regeneration zone of roots 24 hpa in control and 0.5 mM BSO treatment. The y axis is the corrected total cell fluorescence of *pWIP4:GFP* in the new QC domain scaled to render experiments comparable between technical replicates (n = 16 roots, p = 0.05 Wilcoxon test).

(E) Representative images of regenerating root tips stained with mPS-PI to visualize cell walls and amyloplasts 18 hpc. Cells with amyloplasts are pseudo-colored in yellow. The treatments are control, 0.5 mM BSO, 0.5 mM GSH, or combined 0.5 mM BSO + 0.5 mM GSH. Scale bar = 20 μm.

(F) Quantification of the number of cells with amyloplasts in a population of roots from each treatment group shown in E (n = 48 roots, *p < 0.03, Wilcoxon test).

(G) Root tip regeneration rates (y axis) for col-0 (gray) and *cad2-1* (black) seedlings grown on increasing concentrations of BSO (x axis, n > 65 for each treatment group, p value < 0.003, chi-square test).

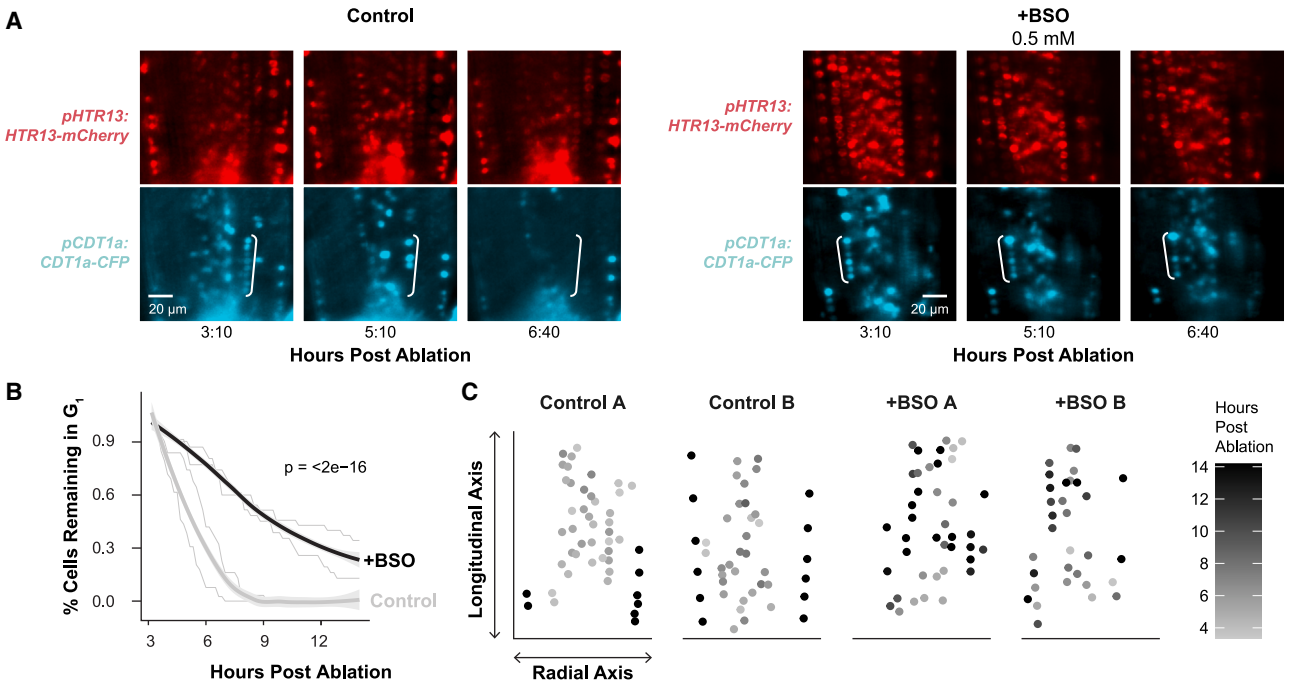

Figure 6. Depletion of GSH with BSO eliminates the coordinated exit from G1 and increases G1 duration in regeneration

(A) Representative images from a control (left) and BSO-treated time-lapse (right) immediately shootward of the ablation site, showing the S (red) and G1 (cyan) markers. Cells from the cortex in G1 are bracketed to highlight the differential disappearance of G1 cells in control versus ablation. S cells are shown to confirm no change in their fluorescent signal. Scale bar = 20 μm.

(B) G1 duration quantified in survivor curves, where cells in G1 were identified in the first frame of the time-lapse and tracked until their transition to S phase for control (gray line) and BSO-treated (black line) time-lapse experiments (p = <2e−16, n = 126 cells, and controls are the same cells shown as "ablated" in Figure 3C, log-rank test).

(C) Grayscale representation of the time in hpa that cells exit G1 mapped onto the given cell's coordinates within the roots, where the Y-intercept represents the ablation site, with two example roots per condition (A and B). Shading scale represents time post-ablation when a cell exited G1.

DISCUSSION

The root has G1 phases with distinct transcriptional modules

Using bulk and scRNA-seq, we defined a set of cell-cycle-phase markers, including a large set of G1 markers, which now provide a resource for the plant community. It has been argued previously that different occurrences of cellular quiescence in plants—meristematic quiescence, dormancy, and terminal differentiation—are controlled distinctly and by non-canonical cell-cycle genes.[36] Our results show that multiple subpopulations of G1 cells exist and are characterized by distinct transcriptional modules. One subpopulation expresses genes relating to cell-wall synthesis, while the other is characterized by genes controlling translation, both of which are functions that are tied to G1 phase in plants.[47,48] Another recent report showed that the longitudinal division speed gradient of the root is largely due to variation in G1 length.[7] Our results support a general model in which the cell cycle is finely tuned to both the maturation stage, as is well-documented, but also to cell identity.

In addition to the ability to detect multiple G1-phase cell populations, we also find evidence for two G2/M populations in our scRNA-seq data, which is supported by our *in vivo* time-lapse data. This indicates our cell-cycle marker set can distinguish cell-cycle sub-phases in Arabidopsis scRNA-seq data and enable further dissection of cell-cycle control in existing and future plant scRNA-seq datasets.

Reprogramming plant cells divide rapidly by shortening G1

In metazoans, evidence links rapid G1 phases with competence to reprogram[49,50]; for example, embryonic stem- and induced-pluripotent cells are characterized by rapid cell cycles with short G1 phases.[49] In plants, while division times in the indeterminately growing meristems are about 20 h,[6] cell division rates during *de novo* root establishment show a dramatic acceleration to 3 to 7 h.[51–53] Here, we show that the fast divisions in regeneration are largely due to a highly truncated G1, similar to observations in reprogramming murine hematopoietic progenitor cells.[50]

In metazoans, G1 has been shown to be a key point in which cells are receptive to cell-fate specialization and differentiation signals.[54–56] Thus, it has been posited that rapid G1s allow cells to remain pluripotent by avoiding differentiation signals.[54–56] In our scRNA-seq profiles, we did not detect any enrichment of known cell identity markers in any specific cell-cycle phase. Thus, we have no evidence that short G1s could bypass differentiation signals, although we cannot rule out that cell-fate markers are induced synchronously but transcribed at different rates or controlled at another level (e.g., Meyer et al.[3] and Winter et al.[4]). Injured roots exposed to a treatment that perturbed rapid

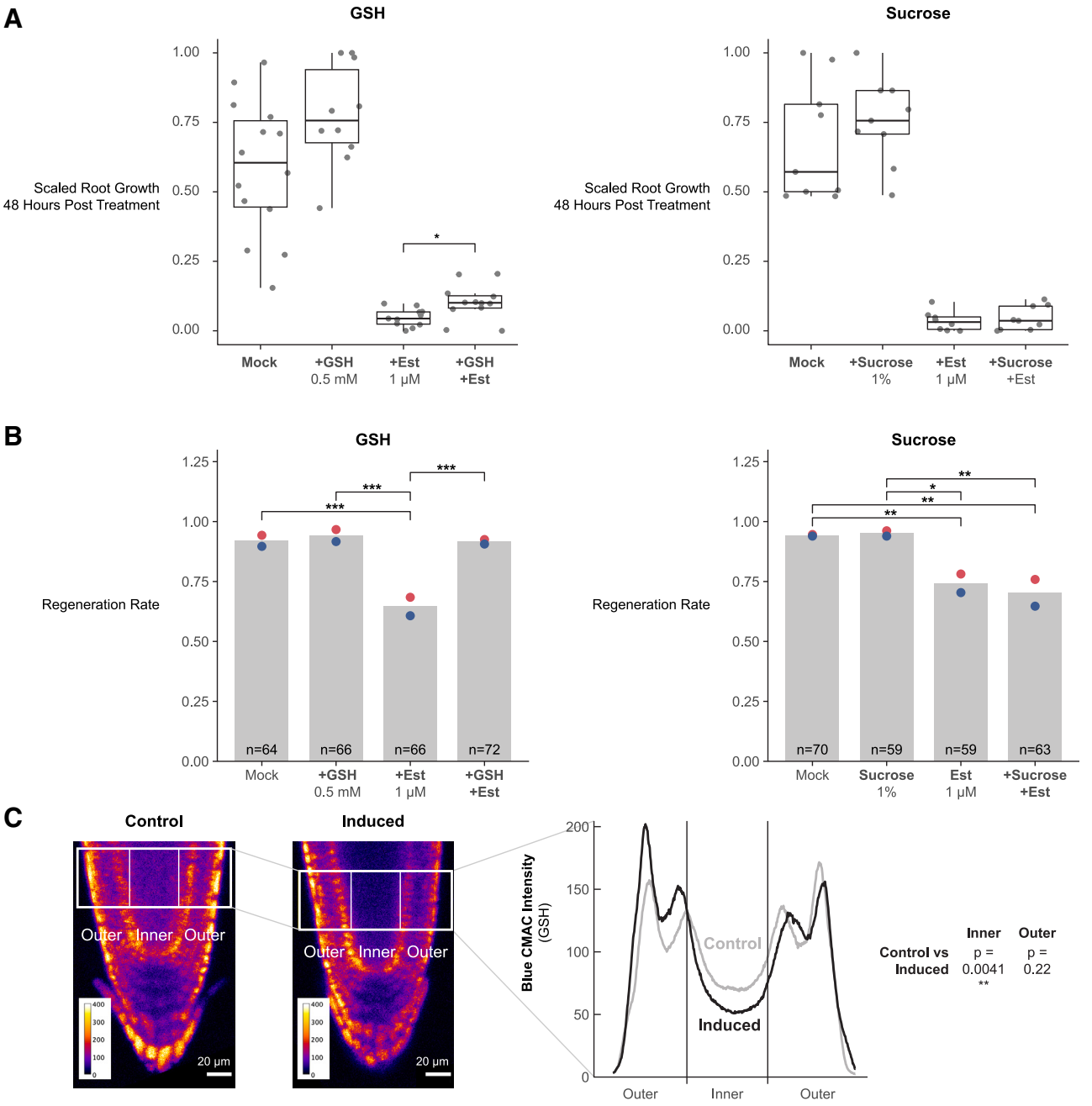

Figure 7. The ground tissue is an apparent source of GSH in homeostatic growth and regeneration

(A) Root growth (y axis) post callose-synthase induction for each treatment condition (x axis). Root lengths are scaled to their own controls within technical replicates to render them comparable across batches. Statistical significance was determined by the pairwise Wilcoxon test comparing estradiol or non-estradiol categories (i.e., mock was tested versus GSH, and estradiol was tested versus estradiol + GSH) ($n > 10$ roots per condition, p value = 0.02).

(B) At left, regeneration rates (y axis) based on the gravitropism test at 48 hpc. The conditions (x axis) are control (mock), GSH-treated roots (+GSH), estradiol-treated roots (+Est), estradiol + GSH-treated roots (+GSH,+Est). At right, the same treatments substituting 1 µM sucrose for GSH. Red and blue dots represent the regeneration rates of technical replicates (***$p < 0.00071$, **$p < 0.0003$, *$p < 0.004$, Fisher's exact test).

(C) In the left panel, representative confocal microscopy images of GSH staining using Blue CMAC for uninduced control (left) and ground-tissue callose-synthase-induced (right) roots are shown. Boxes on the images show representative examples of ROIs used to calculate Blue CMAC intensity on the right panel across inner and outer files. The y axis on the right panel represents the average intensity for each column of pixels of comparable ROIs ($n = 21$) across the x dimension of the ROI. Average intensities for inner versus outer ROIs were tested for significant difference. Only the inner cell files show significant differences between conditions ($p = 0.0041$, pairwise t test). Scale bar = 20 µm.

and coordinated G1s eventually regenerated, so these G1 dynamics potentiate but are not absolutely necessary for cellular reprogramming. Another possible function of rapid G1s is to simply allow a faster entry into S phase. While mechanisms have been identified to link maintenance of histone modifications to DNA replication in plants,[57,58] there is inherent potential for remodeling chromatin during DNA synthesis through new histone deposition,[59] which could mediate cell-fate reprogramming.

Another possibility is that G1 control may simply be the cell's best option to control overall cell cycle, as dictated by environmental context. Several studies have shown that wound responses in plants reflect a bet-hedging strategy that balances defense responses with regenerative growth.[60–63] A similar strategy may have evolved to control cell-cycle speed. Plant stem cells divide infrequently, possibly to limit accumulation of replication-induced mutations.[64] However, wounding creates stresses, such as increased susceptibility to pathogens[65] that require a rapid response. An ability to trigger fast divisions in otherwise slow-dividing cells may have evolved to limit risks of pathogen exposure following wounding. Of course, rapid G1s could have multiple roles in regeneration due to a combination of factors.

G1 cells are primed to perceive tissue damage via GSH nuclear influx

How G1 nuclei maintain higher GSH permeability than nuclei in other cell-cycle phases remains an open question. While there is good evidence that the OLIGOPEPTIDE TRANSPORTER (OPT) family of genes control intercellular GSH transport in plants (reviewed in Lubkowitz[66]) and the CRT (CHLOROQUINE-RESISTANCE TRANSPORTER)-LIKE TRANSPORTER (CLT) family of genes control GSH transport between the cytoplasm and plastids,[67] the mechanism through which GSH is preferentially imported into G1 nuclei in plants is not known.[68] In animals, Bcl-2 has been implicated in GSH nuclear import.[69] However, plants have no apparent orthologs to Bcl-2. Looking forward, identification of the mechanism responsible for mediating GSH transport into G1 nuclei will represent a key link between wound signaling and cell-cycle control in plants.

Regeneration competence is associated with high levels of GSH across kingdoms

Several lines of evidence point to a special role for the endodermis and outer tissues in controlling GSH availability. First, mutants that affect ground-tissue identity, such as *scr* and *shr*, lead to severely stunted roots.[70,71] Our data suggest that another way the endodermis controls growth is as a source of GSH to promote G1 exit and advance the cell cycle. In addition, we implicate a role for the endodermis in regeneration.

The association between GSH levels and regeneration competence is another trait shared across kingdoms. In animals, the liver has the highest capacity to regenerate among solid organs[72] and is the organ with the highest GSH levels.[73] As in root regeneration, liver regeneration is inhibited by perturbation of GSH levels via BSO treatment.[74] Thus, the metabolic environment and core signaling properties of GSH may establish some of the competence of regenerative tissue.

Control of G1 by GSH import and the involvement of fast divisions in pluripotency are remarkably similar facets of regeneration in plants and animals, even if the specific mechanisms have diverged. As efforts are underway in both kingdoms to improve regeneration, the mechanisms that control rapid G1 are promising tools to control the process. Our study points to a remarkably conserved role for GSH in G1 duration and highlights the role of the metabolic environment in regeneration.

Limitations of the study

Several corroborating lines of evidence supported our localization of GSH in the root, and we used multiple methods to validate cell-cycle reporters. Nonetheless, first, we point out that this work relies on dyes to visualize GSH *in vivo* rather than direct visualization. While direct visualization of GSH is possible via mass spectroscopy imaging, the spatial resolution of this technique is not yet fine enough to achieve cell-type-specific resolution in the Arabidopsis root, where many cells are smaller than 10 μm. Further, direct GSH biosensors are not currently available for plants. It will be important to examine GSH localization directly via live imaging when the requisite technology becomes available. In addition, an inducible inhibition of GSH production in the ground tissue would further increase confidence that the ground tissue is the source of GSH to facilitate G1 exit during regeneration. Another limitation relates to our isolation of cells by phase using FACS. In the ideal case, we would have used the cell-cycle readout of PlaCCI using FACS to define cell-cycle phase to obtain bulk protoplast populations using the markers from each phase alone from the same batch of roots. However, we found that the CDT1a and CYCB1;1 fluorescent fusion proteins that mark G1 and G2/M phases in the PlaCCI reporter rapidly diminished in protoplasts. In addition, we could not directly alter G1 duration independently of other mechanisms. The direct manipulation of G1 duration would further show a role for fast G1s in regeneration. When such tools become available, they will be a valuable addition to this literature. Finally, the work does not address how rapid versus slower reprogramming could provide an advantage to the plant. Further work could focus on the ecological or physiological advantages or tradeoffs of rapid cellular reprogramming in regeneration.

RESOURCE AVAILABILITY

Lead contact

Requests for resources or plant lines should be addressed to the lead contact for this work, Kenneth Birnbaum (ken.birnbaum@nyu.edu).

Materials availability

Arabidopsis lines generated for this work are available following publication upon request.

Data and code availability

- Data for scRNA-seq experiments is available under GEO accession GEO: GSE269623. Data for bulk RNA-seq experiments is available under GEO accession GEO: GSE269624.
- This paper does not report original code.

ACKNOWLEDGMENTS

This work was supported by a Postdoctoral Research Fellowship in Biology from the National Science Foundation (2109634) to L.R.L. and a National Institutes of Health grant (R35GM136362) to K.D.B. We acknowledge Dominique

Bergmann, Michael Raissig, Ximena Anleu-Gil, Martin Bringmann, and Joseph Cammarata for helpful discussions.

AUTHOR CONTRIBUTIONS

L.R.L.: conceptualization, methodology, validation, formal analysis, investigation, writing – original draft, writing – review & editing, and visualization. B.G.: resources, data curation, writing – review & editing. R.R.: investigation, writing – review & editing, and visualization. C.H.: investigation. B.D.: resources and writing – review & editing. C.G.: resources and writing – review & editing. K.D.B.: conceptualization, methodology, writing – original draft, writing – review & editing, supervision, and funding acquisition.

DECLARATION OF INTERESTS

The authors declare no competing interests.

STAR★METHODS

Detailed methods are provided in the online version of this paper and include the following:

- KEY RESOURCES TABLE
- EXPERIMENTAL MODEL AND STUDY PARTICIPANTS
  - Plant growth and treatment conditions
- METHOD DETAILS
  - Confocal microscopy
  - Light Sheet Microscopy
  - scRNA-seq
  - Bulk RNA-seq
  - Sequencing Data Analysis
  - Imaging Data Analysis
  - *In Situ* Hybridization
- QUANTIFICATION AND STATISTICAL ANALYSIS

SUPPLEMENTAL INFORMATION

Supplemental information can be found online at https://doi.org/10.1016/j.devcel.2024.12.019.

Received: June 17, 2024
Revised: October 1, 2024
Accepted: December 10, 2024
Published: January 3, 2025

REFERENCES

1. Hall, R.D., Riksen-Bruinsma, T., Weyens, G., Lefebvre, M., Dunwell, J.M., and Krens, F.A. (1996). Stomatal Guard Cells Are Totipotent. Plant Physiol. *112*, 889–892. https://doi.org/10.1104/pp.112.3.889.
2. Sena, G., Wang, X., Liu, H.-Y., Hofhuis, H., and Birnbaum, K.D. (2009). Organ regeneration does not require a functional stem cell niche in plants. Nature *457*, 1150–1153. https://doi.org/10.1038/nature07597.
3. Meyer, H.M., Teles, J., Formosa-Jordan, P., Refahi, Y., San-Bento, R., Ingram, G., Jönsson, H., Locke, J.C.W., and Roeder, A.H.K. (2017). Fluctuations of the transcription factor atml1 generate the pattern of giant cells in the arabidopsis sepal. eLife *6*, e19131. https://doi.org/10.7554/eLife.19131.001.
4. Winter, C.M., Szekely, P., Popov, V., Belcher, H., Carter, R., Jones, M., Fraser, S.E., Truong, T.V., and Benfey, P.N. (2024). SHR and SCR coordinate root patterning and growth early in the cell cycle. Nature *626*, 611–616. https://doi.org/10.1038/s41586-023-06971-z.
5. Lee, L.R., and Bergmann, D.C. (2019). The plant stomatal lineage at a glance. J. Cell Sci. *132*, jcs228551. https://doi.org/10.1242/jcs.228551.
6. Rahni, R., and Birnbaum, K.D. (2019). Week-long imaging of cell divisions in the Arabidopsis root meristem. Plant Methods *15*, 30. https://doi.org/10.1186/s13007-019-0417-9.
7. Echevarria, C., Desvoyes, B., Marconi, M., Franco-Zorrila, J.M., Lee, L., Umeda, M., Sablowski, R., Birnbaum, K.D., Wabnik, K., and Gutierrez, C. (2022). Stem cell regulators control a G1 duration gradient in the plant root meristem. Preprint at bioRxiv. https://doi.org/10.1101/2022.03.09.483577.
8. Han, S.-K., Herrmann, A., Yang, J., Iwasaki, R., Sakamoto, T., Desvoyes, B., Kimura, S., Gutierrez, C., Kim, E.-D., and Torii, K.U. (2022). Deceleration of the cell cycle underpins a switch from proliferative to terminal divisions in plant stomatal lineage. Dev. Cell *57*, 569–582.e6. https://doi.org/10.1016/j.devcel.2022.01.014.
9. Liu, L., Michowski, W., Kolodziejczyk, A., and Sicinski, P. (2019). The cell cycle in stem cell proliferation, pluripotency and differentiation. Nat. Cell Biol. *21*, 1060–1067. https://doi.org/10.1038/s41556-019-0384-4.
10. Hu, X., Eastman, A.E., and Guo, S. (2019). Cell cycle dynamics in the reprogramming of cellular identity. FEBS Lett. *593*, 2840–2852. https://doi.org/10.1002/1873-3468.13625.
11. Soufi, A., and Dalton, S. (2016). Cycling through developmental decisions: how cell cycle dynamics control pluripotency, differentiation and reprogramming. Development *143*, 4301–4311. https://doi.org/10.1242/dev.142075.
12. Zaveri, L., and Dhawan, J. (2018). Cycling to Meet Fate: Connecting Pluripotency to the Cell Cycle. Front. Cell Dev. Biol. *6*, 57. https://doi.org/10.3389/fcell.2018.00057.
13. Sablowski, R., and Gutierrez, C. (2022). Cycling in a crowd: Coordination of plant cell division, growth, and cell fate. Plant Cell *34*, 193–208. https://doi.org/10.1093/plcell/koab222.
14. Desvoyes, B., and Gutierrez, C. (2020). Roles of plant retinoblastoma protein: cell cycle and beyond. EMBO J. *39*, e105802. https://doi.org/10.15252/embj.2020105802.
15. Gutierrez, C. (2016). 25 Years of Cell Cycle Research: What's Ahead? Trends Plant Sci. *21*, 823–833. https://doi.org/10.1016/j.tplants.2016.06.007.
16. Sozzani, R., Cui, H., Moreno-Risueno, M.A., Busch, W., Van Norman, J.M., Vernoux, T., Brady, S.M., Dewitte, W., Murray, J.A.H., and Benfey, P.N. (2010). Spatiotemporal regulation of cell-cycle genes by SHORTROOT links patterning and growth. Nature *466*, 128–132. https://doi.org/10.1038/nature09143.
17. Weimer, A.K., Matos, J.L., Sharma, N., Patell, F., Murray, J.A.H., Dewitte, W., and Bergmann, D.C. (2018). Lineage- and stage-specific expressed CYCD7;1 coordinates the single symmetric division that creates stomatal guard cells. Development *145*, dev160671. https://doi.org/10.1242/dev.160671.
18. Han, S.-K., Qi, X., Sugihara, K., Dang, J.H., Endo, T.A., Miller, K.L., Kim, E.-D., Miura, T., and Torii, K.U. (2018). MUTE Directly Orchestrates Cell-State Switch and the Single Symmetric Division to Create Stomata. Dev. Cell *45*, 303–315.e5. https://doi.org/10.1016/J.DEVCEL.2018.04.010.
19. Menges, M., and Murray, J.A.H. (2002). Synchronous Arabidopsis suspension cultures for analysis of cell-cycle gene activity. Plant J. *30*, 203–212. https://doi.org/10.1046/j.1365-313x.2002.01274.x.
20. Menges, M., De Jager, S.M., Gruissem, W., and Murray, J.A.H. (2005). Global analysis of the core cell cycle regulators of Arabidopsis identifies novel genes, reveals multiple and highly specific profiles of expression and provides a coherent model for plant cell cycle control. Plant J. *41*, 546–566. https://doi.org/10.1111/j.1365-313X.2004.02319.x.
21. Diehl, F.F., Sapp, K.M., and Vander Heiden, M.G. (2024). The bidirectional relationship between metabolism and cell cycle control. Trends Cell Biol. *34*, 136–149. https://doi.org/10.1016/j.tcb.2023.05.012.
22. Zhang, T., Noll, S.E., Peng, J.T., Klair, A., Tripka, A., Stutzman, N., Cheng, C., Zare, R.N., and Dickinson, A.J. (2023). Chemical imaging reveals diverse functions of tricarboxylic acid metabolites in root growth and development. Nat. Commun. *14*, 2567. https://doi.org/10.1038/s41467-023-38150-z.

23. Tsukagoshi, H., Busch, W., and Benfey, P.N. (2010). Transcriptional regulation of ROS controls transition from proliferation to differentiation in the root. Cell *143*, 606–616. https://doi.org/10.1016/j.cell.2010.10.020.

24. Ribas, V., García-Ruiz, C., and Fernández-Checa, J.C. (2014). Glutathione and mitochondria. Front. Pharmacol. *5*, 151. https://doi.org/10.3389/fphar.2014.00151.

25. Diaz Vivancos, P., Wolff, T., Markovic, J., Pallardó, F.V., and Foyer, C.H. (2010). A nuclear glutathione cycle within the cell cycle. Biochem. J. *431*, 169–178. https://doi.org/10.1042/BJ20100409.

26. Vernoux, T., Wilson, R.C., Seeley, K.A., Reichheld, J.P., Muroy, S., Brown, S., Maughan, S.C., Cobbett, C.S., Van Montagu, M., Inzé, D., et al. (2000). The ROOT MERISTEMLESS1/CADMIUM SENSITIVE2 gene defines a glutathione-dependent pathway involved in initiation and maintenance of cell division during postembryonic root development. Plant Cell *12*, 97–110. https://doi.org/10.1105/tpc.12.1.97.

27. Vivancos, P.D., Dong, Y., Ziegler, K., Markovic, J., Pallardó, F.V., Pellny, T.K., Verrier, P.J., and Foyer, C.H. (2010). Recruitment of glutathione into the nucleus during cell proliferation adjusts whole-cell redox homeostasis in Arabidopsis thaliana and lowers the oxidative defense shield. Plant J. *64*, 825–838. https://doi.org/10.1111/j.1365-313X.2010.04371.x.

28. Koprivova, A., Mugford, S.T., and Kopriva, S. (2010). Arabidopsis root growth dependence on glutathione is linked to auxin transport. Plant Cell Rep. *29*, 1157–1167. https://doi.org/10.1007/s00299-010-0902-0.

29. de Simone, A., Hubbard, R., de la Torre, N.V., Velappan, Y., Wilson, M., Considine, M.J., Soppe, W.J.J., and Foyer, C.H. (2017). Redox Changes During the Cell Cycle in the Embryonic Root Meristem of Arabidopsis thaliana. Antioxid. Redox Signal. *27*, 1505–1519. https://doi.org/10.1089/ars.2016.6959.

30. Cools, T., Iantcheva, A., Maes, S., Van den Daele, H., and De Veylder, L. (2010). A replication stress-induced synchronization method for Arabidopsis thaliana root meristems. Plant J. *64*, 705–714. https://doi.org/10.1111/j.1365-313X.2010.04361.x.

31. Hao, Y., Hao, S., Andersen-Nissen, E., Mauck, W.M., 3rd, Zheng, S., Butler, A., Lee, M.J., Wilk, A.J., Darby, C., Zager, M., et al. (2021). Integrated analysis of multimodal single-cell data. Cell *184*, 3573–3587.e29. https://doi.org/10.1016/j.cell.2021.04.048.

32. Fragkos, M., Ganier, O., Coulombe, P., and Méchali, M. (2015). DNA replication origin activation in space and time. Nat. Rev. Mol. Cell Biol. *16*, 360–374. https://doi.org/10.1038/nrm4002.

33. Okada, T., Endo, M., Singh, M.B., and Bhalla, P.L. (2005). Analysis of the histone H3 gene family in Arabidopsis and identification of the male-gamete-specific variant AtMGH3. Plant J. *44*, 557–568. https://doi.org/10.1111/j.1365-313X.2005.02554.x.

34. Rahni, R., Guillotin, B., Lee, L.R., and Birnbaum, K.D. (2024). A temporal map of division, chromatin modification, and identity specification in the regenerating root. Preprint at bioRxiv. https://doi.org/10.1101/2024.01.09.574680.

35. Bizet, F., Hummel, I., and Bogeat-Triboulot, M.-B. (2015). Length and activity of the root apical meristem revealed in vivo by infrared imaging. J. Exp. Bot. *66*, 1387–1395. https://doi.org/10.1093/jxb/eru488.

36. Velappan, Y., Signorelli, S., and Considine, M.J. (2017). Cell cycle arrest in plants: what distinguishes quiescence, dormancy and differentiated G1? Ann. Bot. *120*, 495–509. https://doi.org/10.1093/aob/mcx082.

37. Desvoyes, B., Arana-Echarri, A., Barea, M.D., and Gutierrez, C. (2020). A comprehensive fluorescent sensor for spatiotemporal cell cycle analysis in Arabidopsis. Nat. Plants *6*, 1330–1334. https://doi.org/10.1038/s41477-020-00770-4.

38. Nawy, T., Lee, J.-Y., Colinas, J., Wang, J.Y., Thongrod, S.C., Malamy, J.E., Birnbaum, K., and Benfey, P.N. (2005). Transcriptional profile of the Arabidopsis root quiescent center. Plant Cell *17*, 1908–1925. https://doi.org/10.1105/tpc.105.031724.

39. Prasad, A., Sedlářová, M., Balukova, A., Rác, M., and Pospíšil, P. (2019). Reactive Oxygen Species as a Response to Wounding: In Vivo Imaging in Arabidopsis thaliana. Front. Plant Sci. *10*, 1660. https://doi.org/10.3389/fpls.2019.01660.

40. Zhang, H., Zhang, T.T., Liu, H., Shi, Y., Wang, M., Bie, X.M., Li, X.G., and Zhang, X.S. (2018). Thioredoxin-mediated ROS Homeostasis Explains natural variation in plant regeneration. Plant Physiol. *176*, 2231–2250. https://doi.org/10.1104/pp.17.00633.

41. Arisi, A.C., Noctor, G., Foyer, C.H., and Jouanin, L. (1997). Modification of thiol contents in poplars (Populus tremula x P. alba) overexpressing enzymes involved in glutathione synthesis. Planta *203*, 362–372. https://doi.org/10.1007/s004250050202.

42. Truernit, E., Bauby, H., Dubreucq, B., Grandjean, O., Runions, J., Barthélémy, J., and Palauqui, J.-C. (2008). High-resolution whole-mount imaging of three-dimensional tissue organization and gene expression enables the study of Phloem development and structure in Arabidopsis. Plant Cell *20*, 1494–1503. https://doi.org/10.1105/tpc.107.056069.

43. Cobbett, C.S., May, M.J., Howden, R., and Rolls, B. (1998). The glutathione-deficient, cadmium-sensitive mutant, cad2-1, of Arabidopsis thaliana is deficient in gamma-glutamylcysteine synthetase. Plant J. *16*, 73–78. https://doi.org/10.1046/j.1365-313x.1998.00262.x.

44. Plantin-Carrenard, E., Braut-Boucher, F., Bernard, M., Derappe, C., Foglietti, M.J., and Aubery, M. (2000). Fluorogenic Probes Applied to the Study of Induced Oxidative Stress in the Human Leukemic HL60 Cell Line. J. Fluoresc. *10*, 167. https://doi.org/10.1023/A:1009499210857.

45. Toyota, M., Spencer, D., Sawai-Toyota, S., Jiaqi, W., Zhang, T., Koo, A.J., Howe, G.A., and Gilroy, S. (2018). Glutamate triggers long-distance, calcium-based plant defense signaling. Science *361*, 1112–1115. https://doi.org/10.1126/science.aat7744.

46. Vatén, A., Dettmer, J., Wu, S., Stierhof, Y.-D., Miyashima, S., Yadav, S.R., Roberts, C.J., Campilho, A., Bulone, V., Lichtenberger, R., et al. (2011). Callose biosynthesis regulates symplastic trafficking during root development. Dev. Cell *21*, 1144–1155. https://doi.org/10.1016/j.devcel.2011.10.006.

47. Sablowski, R., and Carnier Dornelas, M. (2014). Interplay between cell growth and cell cycle in plants. J. Exp. Bot. *65*, 2703–2714. https://doi.org/10.1093/jxb/ert354.

48. Soni, N., and Bacete, L. (2023). The interplay between cell wall integrity and cell cycle progression in plants. Plant Mol. Biol. *113*, 367–382. https://doi.org/10.1007/s11103-023-01394-w.

49. Ruiz, S., Panopoulos, A.D., Herrerías, A., Bissig, K.-D., Lutz, M., Berggren, W.T., Verma, I.M., and Izpisua Belmonte, J.C. (2011). A high proliferation rate is required for cell reprogramming and maintenance of human embryonic stem cell identity. Curr. Biol. *21*, 45–52. https://doi.org/10.1016/j.cub.2010.11.049.

50. Guo, S., Zi, X., Schulz, V.P., Cheng, J., Zhong, M., Koochaki, S.H.J., Megyola, C.M., Pan, X., Heydari, K., Weissman, S.M., et al. (2014). Nonstochastic reprogramming from a privileged somatic cell state. Cell *156*, 649–662. https://doi.org/10.1016/j.cell.2014.01.020.

51. Gooh, K., Ueda, M., Aruga, K., Park, J., Arata, H., Higashiyama, T., and Kurihara, D. (2015). Live-cell imaging and optical manipulation of Arabidopsis early embryogenesis. Dev. Cell *34*, 242–251. https://doi.org/10.1016/j.devcel.2015.06.008.

52. Dubrovsky, J.G., Rost, T.L., Colón-Carmona, A., and Doerner, P. (2001). Early primordium morphogenesis during lateral root initiation in Arabidopsis thaliana. Planta *214*, 30–36. https://doi.org/10.1007/s004250100598.

53. Rahni, R. (2020). Re: Generation of Identity and Stem Cell Activity in the Arabidopsis Root. PhD thesis (New York University).

54. Pauklin, S., and Vallier, L. (2013). The cell-cycle state of stem cells determines cell fate propensity. Cell *155*, 135–147. https://doi.org/10.1016/j.cell.2013.08.031.

55. Singh, A.M., Chappell, J., Trost, R., Lin, L., Wang, T., Tang, J., Wu, H., Zhao, S., Jin, P., and Dalton, S. (2013). Cell-Cycle Control of Developmentally Regulated Transcription Factors Accounts for

Heterogeneity in Human Pluripotent Cells. Stem Cell Rep. *1*, 532–544. https://doi.org/10.1016/J.STEMCR.2013.10.009.

56. Dalton, S. (2015). Linking the Cell Cycle to Cell Fate Decisions. Trends Cell Biol. *25*, 592–600. https://doi.org/10.1016/J.TCB.2015.07.007.
57. Jiang, D., and Berger, F. (2017). DNA replication–coupled histone modification maintains Polycomb gene silencing in plants. Science *357*, 1146–1149. https://doi.org/10.1126/science.aan4965.
58. Yang, H., Berry, S., Olsson, T.S.G., Hartley, M., Howard, M., and Dean, C. (2017). Distinct phases of Polycomb silencing to hold epigenetic memory of cold in Arabidopsis. Science *357*, 1142–1145. https://doi.org/10.1126/science.aan1121.
59. MacAlpine, D.M., and Almouzni, G. (2013). Chromatin and DNA replication. Cold Spring Harb. Perspect. Biol. *5*, a010207. https://doi.org/10.1101/cshperspect.a010207.
60. Hernández-Coronado, M., Dias Araujo, P.C., Ip, P.-L., Nunes, C.O., Rahni, R., Wudick, M.M., Lizzio, M.A., Feijó, J.A., and Birnbaum, K.D. (2022). Plant glutamate receptors mediate a bet-hedging strategy between regeneration and defense. Dev. Cell *57*, 451–465.e6. https://doi.org/10.1016/j.devcel.2022.01.013.
61. Züst, T., and Agrawal, A.A. (2017). Trade-Offs Between Plant Growth and Defense Against Insect Herbivory: An Emerging Mechanistic Synthesis. Annu. Rev. Plant Biol. *68*, 513–534. https://doi.org/10.1146/annurev-arplant-042916-040856.
62. Guo, Q., Yoshida, Y., Major, I.T., Wang, K., Sugimoto, K., Kapali, G., Havko, N.E., Benning, C., and Howe, G.A. (2018). JAZ repressors of metabolic defense promote growth and reproductive fitness in Arabidopsis. Proc. Natl. Acad. Sci. USA *115*, E10768–E10777. https://doi.org/10.1073/pnas.1811828115.
63. Huot, B., Yao, J., Montgomery, B.L., and He, S.Y. (2014). Growth-defense tradeoffs in plants: a balancing act to optimize fitness. Mol. Plant *7*, 1267–1287. https://doi.org/10.1093/mp/ssu049.
64. Burian, A., Barbier de Reuille, P., and Kuhlemeier, C. (2016). Patterns of Stem Cell Divisions Contribute to Plant Longevity. Curr. Biol. *26*, 1385–1394. https://doi.org/10.1016/j.cub.2016.03.067.
65. Savatin, D.V., Gramegna, G., Modesti, V., and Cervone, F. (2014). Wounding in the plant tissue: the defense of a dangerous passage. Front. Plant Sci. *5*, 470. https://doi.org/10.3389/fpls.2014.00470.
66. Lubkowitz, M. (2011). The oligopeptide transporters: a small gene family with a diverse group of substrates and functions? Mol. Plant *4*, 407–415. https://doi.org/10.1093/mp/ssr004.
67. Maughan, S.C., Pasternak, M., Cairns, N., Kiddle, G., Brach, T., Jarvis, R., Haas, F., Nieuwland, J., Lim, B., Müller, C., et al. (2010). Plant homologs of the *Plasmodium falciparum* chloroquine-resistance transporter, *Pf*CRT, are required for glutathione homeostasis and stress responses. Proc. Natl. Acad. Sci. USA *107*, 2331–2336. https://doi.org/10.1073/pnas.0913689107.
68. Noctor, G., Queval, G., Mhamdi, A., Chaouch, S., and Foyer, C.H. (2011). Glutathione. Arabidopsis Book *9*, e0142. https://doi.org/10.1199/tab.0142.
69. Voehringer, D.W., McConkey, D.J., McDonnell, T.J., Brisbay, S., and Meyn, R.E. (1998). Bcl-2 expression causes redistribution of glutathione to the nucleus. Proc. Natl. Acad. Sci. USA *95*, 2956–2960. https://doi.org/10.1073/pnas.95.6.2956.
70. Di Laurenzio, L., Wysocka-Diller, J., Malamy, J.E., Pysh, L., Helariutta, Y., Freshour, G., Hahn, M.G., Feldmann, K.A., and Benfey, P.N. (1996). The SCARECROW gene regulates an asymmetric cell division that is essential for generating the radial organization of the Arabidopsis root. Cell *86*, 423–433. https://doi.org/10.1016/s0092-8674(00)80115-4.
71. Helariutta, Y., Fukaki, H., Wysocka-Diller, J., Nakajima, K., Jung, J., Sena, G., Hauser, M.T., and Benfey, P.N. (2000). The SHORT-ROOT gene controls radial patterning of the Arabidopsis root through radial signaling. Cell *101*, 555–567. https://doi.org/10.1016/s0092-8674(00)80865-x.
72. Michalopoulos, G.K., and DeFrances, M.C. (1997). Liver regeneration. Science *276*, 60–66. https://doi.org/10.1126/science.276.5309.60.
73. Ookhtens, M., and Kaplowitz, N. (1998). Role of the liver in interorgan homeostasis of glutathione and cyst(e)ine. Semin. Liver Dis. *18*, 313–329. https://doi.org/10.1055/s-2007-1007167.
74. Huang, Z.Z., Chen, C., Zeng, Z., Yang, H., Oh, J., Chen, L., and Lu, S.C. (2001). Mechanism and significance of increased glutathione level in human hepatocellular carcinoma and liver regeneration. FASEB J. *15*, 19–21. https://doi.org/10.1096/fj.00-0445fje.
75. Guillotin, B., Rahni, R., Passalacqua, M., Mohammed, M.A., Xu, X., Raju, S.K., Ramírez, C.O., Jackson, D., Groen, S.C., Gillis, J., et al. (2023). A pan-grass transcriptome reveals patterns of cellular divergence in crops. Nature *617*, 785–791. https://doi.org/10.1038/s41586-023-06053-0.
76. Bargmann, B.O.R., and Birnbaum, K.D. (2010). Fluorescence Activated Cell Sorting of Plant Protoplasts. J. Vis. Exp. *2–5*, 1673. https://doi.org/10.3791/1673.
77. Lee, L.R., Wengier, D.L., and Bergmann, D.C. (2019). Cell-type–specific transcriptome and histone modification dynamics during cellular reprogramming in the Arabidopsis stomatal lineage. Proc. Natl. Acad. Sci. USA *116*, 21914–21924. https://doi.org/10.1073/pnas.1911400116.
78. Hafemeister, C., and Satija, R. (2019). Normalization and variance stabilization of single-cell RNA-seq data using regularized negative binomial regression. Genome Biol. *20*, 296. https://doi.org/10.1186/s13059-019-1874-1.
79. Bewick, V., Cheek, L., and Ball, J. (2004). Statistics review 12: survival analysis. Crit. Care *8*, 389–394. https://doi.org/10.1186/cc2955.
80. Huang, T., Guillotin, B., Rahni, R., Birnbaum, K.D., and Wagner, D. (2023). A rapid and sensitive, multiplex, whole mount RNA fluorescence in situ hybridization and immunohistochemistry protocol. Plant Methods *19*, 131. https://doi.org/10.1186/s13007-023-01108-9.
81. Therneau, T. (2024). A Package for Survival Analysis in R. R package version 3.7-0, https://CRAN.R-project.org/package=survival.
82. Erdman, C., and Emerson, J.W. (2007). Bcp: An R Package for performing a Bayesian analysis of change point problems. J. Stat. Soft. *23*, 1–13. https://doi.org/10.18637/jss.v023.i03.

STAR★METHODS

KEY RESOURCES TABLE

REAGENT or RESOURCE	SOURCE	IDENTIFIER
Chemicals, Peptides, and Recombinant Proteins		
L-Glutathione reduced	Millipore Sigma	G6013
Invitrogen™ CellTracker™ Blue CMAC Dye	Fisher Scientific	C2925
Invitrogen™ CellTracker™ Green CMFDA Dye	Fisher Scientific	C2925
Invitrogen™ H2DCFDA (H2-DCF, DCF)	Fisher Scientific	D399
L-BUTHIONINE-(S,R)-SULFOXIMINE	Millipore Sigma	B2515
HYDROXYUREA, 98%, POWDER	Millipore Sigma	H8627
Critical Commercial Assays		
Chromium Next GEM Single Cell 3' Reagent Kit v3.1	10X Genomics	PN-1000121
Ovation Ultralow Library System V2	Tecan	Part No. 0344
SMART-Seq v4 full-length transcriptome analysis kit	Takara	product # 634888
RNA micro kit	Qiagen	74004
D1000 ScreenTape	Agilent	5067-5582
D1000 Reagents	Agilent	5067-5583
Qubit HS dsDNA	Thermofischer	Q32851
High Sensitivity RNA ScreenTape	Agilent	5067-5579
High Sensitivity RNA ScreenTape Ladder	Agilent	5067-5581
High Sensitivity RNA ScreenTape Sample Buffer	Agilent	5067-5580
High Sensitivity D5000 ScreenTape	Agilent	5067-5592
High Sensitivity D5000 Reagents	Agilent	5067-5593
Deposited Data		
scRNA-seq data	NA	GEO: GSE269623
bulk RNA-seq data	NA	GEO: GSE269624
Experimental Models: Organisms/Strains		
Arabidopsis thaliana	NA	RRID:NCBITaxon_3702
Software and Algorithms		
Imaris	Oxford Instruments	RRID: SCR_007370
Seurat	Bioconductor	RRID: SCR_007322
Monocle3	Bioconductor	RRID: SCR_018685
FIJI	ImageJ.net	RRID: SCR_002285
Zen Black	Zeiss	RRID: SCR_018163

EXPERIMENTAL MODEL AND STUDY PARTICIPANTS

Plant growth and treatment conditions

Arabidopsis col-0 seedlings were grown vertically in an incubator set to long day conditions on ½ MS media unless otherwise noted. For hydroxyurea (HU) treatment, seedlings were synchronized in one of three cell cycle phases as previously described.[30] Briefly, seedlings were grown until 6 DPG vertically on ½ MS on top of sterile mesh (product #03100/32, ELKO Filtering Systems). Then seedlings were transferred to MS plates supplemented with 2mM HU (product # H8627, Millipore Sigma). Various incubation times were used to synchronize cells in different phases of the cell cycle as follows: 6 hr for S phase, 17 hr for G2/M, and 22 hr for G1. Synchronization in each phase was confirmed via confocal microscopy using the PlaCCI reporter. For BSO treatment, seedlings were germinated on MS media alone (control) or supplemented with 1 or 0.5 mM BSO (product # B2515, Millipore Sigman) as previously described.[28] Seedlings were grown vertically on this media until they were 7 DPG and then used for either imaging or regeneration assays. Regeneration assays were performed by manually removing the distal-most 70 microns of the root tip using an ophthalmic scalpel (product #72045-15, Feather Safety Razor Company). Roots were then allowed to grow while regeneration was monitored by either staining for amyloplasts at 18 hr with mPS-PI[42] or by counting the proportion of roots that had recovered gravitropism at 48 hr.[2] PlaCCI seedlings (*pCDT1a:CDT1a-eCFP*, *pHTR13:HTR13-mCherry* and *pCYCB1;1:NCYCB1;1-YFP*, where "N" denotes

an N terminal fusion) were crossed to cell type reporters including *pWIP4:GFP* (columella and QC), *pWOX5:YFP* (QC), *PET111:YFP* (mature columella), and *pSCR:erYFP* (endodermis and QC). An estradiol inducible callose synthase line[46] driving induction in the cortex and endodermis was used for plasmodesmatal block experiments. For these experiments, plants were grown vertically on sterile mesh on top of ½ MS for 7 days, then transferred to ½ MS supplemented with 1 μM estradiol for 17 hr. Where noted, estradiol plates also included GSH (0.5mM) or sucrose (1%). Plants were then transferred back to unsupplemented ½ MS. Regeneration experiments were then performed as described above. For root growth experiments, root tip locations were marked after transfer back to ½ MS and then growth from that point was measured 24 hr later.

All experiments, unless otherwise noted, were performed on seedlings at 7 dpg.

METHOD DETAILS

Confocal microscopy

Multichannel imaging was performed on a Zeiss 880 Airyscan microscope. Channel acquisition parameters were initially defined using the Zen Smart Setup feature and then refined to ensure the acquisition range was narrow and centered over the emission peak. Channels were then acquired in sequential scans to maximize signal and minimize spectral overlap.

In the root tip regeneration system, the meristem is excised, completely removing the QC and columella cells, which are then respecified within a day from vascular and other cells left in the cut stump.[2] To enable rapid imaging after regeneration, we generated a similar root-tip excision using a two-photon ablation system in which the root meristem is essentially isolated by a plane of dead cells causing regeneration of QC and columella shootward, as in root tip excision. Laser ablations that were sufficient to cause new meristem establishment (regeneration) were performed using a Coherent Chameleon Vision II 2-photon laser on a Zeiss 880 Airyscan microscope. A 2-dimensional ROI was specified using the Zeiss ROI manager in the Zen Acquisition Black software with the time series, bleaching, and ROI modes enabled. This ROI targeted a transverse section of the root that was positioned approximately 10-20 microns shootward of the QC that spanned the entire medio-lateral dimension of the root with a thickness of approximately 5-10 microns. The ablation laser was used at 710 nm at 100 percent power for 15 iterations. In order to ensure sufficient tissue damage was achieved to induce the root to establish a new meristem, the ablation was performed in 3 Z planes: (1) in the medial plane, and then on both sides of the medial plane (2) closer to the cover slip and targeting the epidermis and cortex (about 15-20 microns off the medial plane), and (3) further from the cover slip than the median plane as deep as the confocal microscope could image into the tissue before imaging quality degraded (15-20 microns from the medial plane). Each ablation was performed as part of a time lapse acquisition, in which typically two frames were acquired, followed by the ablation, and then three additional frames were acquired. These frames were set to be acquired 1 millisecond apart, which functionally resulted in continuous acquisitions and total time lapses of approximately 90 seconds. For 30-minute-long time lapses taken on the Zeiss 880 Airyscan confocal, frames were acquired in one Z plane three minutes apart. This laser ablation strategy was adopted to enable imaging of injured roots that were already mounted in a cuvette compatible with our light sheet setup (described below) so that we could monitor injury response via time lapse microscopy without any confounding effects of the stress of mounting seedlings after root tip removal.

Plants were stained with Blue CMAC by mounting in imaging cuvettes as described above using media supplemented with Blue CMAC (ThermoFisher #C2110) to achieve a concentration of 10 μM once the media had equilibrated to 30 degrees Celsius. Media was then split into a number of batches equal to the number of treatment conditions to ensure that all conditions received the same concentration of Blue CMAC. Additional treatments were then supplemented into the relevant batch of media as required. 5 mL of each media treatment was then added to its own cuvette and cured for at least four hr at 4 degrees Celsius. Plants were then transferred to an imaging cuvette and allowed to recover in the growth chamber overnight. For CMFDA and H2DCFDA staining, seedlings were transferred to liquid ½ MS supplemented with either stain to a final concentration of 1 μM for 1 hr prior to imaging.

Light Sheet Microscopy

All time lapse movies were performed on an inverted Leica model Dmi8 outfitted with a Tilt Light Sheet Imaging System (Mizar) with filters optimized to visualization of YFP, CFP, and mCherry (Chroma). All roots were imaged at 7 dpg. Samples were mounted for light sheet microscopy as follows: plants were grown vertically on MS plates for 6 days. On day 6, 5 mL of MS with 2% low melt agarose was cast into imaging cuvettes (CellVis product number #C1-1.5H-N) after being filtered through a 0.45 micron nylon filter (product # 76479-042, VWR) to remove any particulates that might disturb the path of the light sheet to prepare media ''blankets''. These blankets were stored at 4 degrees Celsius for at least four hr prior to mounting to ensure they had fully polymerized. A sterile scalpel and forceps were used to remove a small amount of media from one end of the cuvette to create a gap that could be used to lift the media out of the cuvette. The scalpel was then gently run along the edge of the imaging chamber to free the blanket while producing minimal distortions to the media. Sterile canted forceps were then used to gently lift the media blanket out of the cuvette and placed in a sterile petri dish. Several 6 DPG seedlings were placed on top of the media blanket such that the roots were in contact with the blanket and the shoots hung off the edge. A fresh cuvette was then lowered over the blanket until the blanket made contact with the cover slip at the bottom of the cuvette. Seedlings were inspected for tissue damage under a brightfield microscope and any gaps between the blanket and the wall of the cuvette were filled in with additional filtered media prepared as above to ensure the light sheet did not pass through any air gaps. The assembled cuvettes were then placed into a growth chamber overnight oriented such that the roots pointed downward to allow the plants to recover from the stress of the mounting procedure. Roots were imaged with a 40X water

immersion objective, with stacks spanning the entire Z dimension spaced 1.5 microns apart acquired every ten minutes in mCherry, CFP, and YFP to create time lapse movies of PlaCCI. Laser power and acquisition time was adjusted for each experiment to account for variable distance of the sample to the side of the cuvette through which the light sheet enters. A sample binning of 2 was used to improve signal brightness. For imaging of the F3 progeny of PlaCCI crossed to the WIP4 transcriptional reporter or the *PET111:YFP* enhancer trap line[38] in which both transgenes had been screened for stable brightness, a fourth channel - GFP - was imaged. No photobleaching was observed using these imaging conditions over the course of a time lapse. To maintain imaging quality, water was added to the 40X objective after 7-10 hr of imaging depending on the ambient humidity. This was accomplished by briefly removing the imaging cuvette between acquisitions, adding additional water to the objective, and then replacing the cuvette. The stage was adjusted to recenter the sample and then the image was realigned *post hoc* using Imaris to account for any subtle shifts in sample position. This allowed us to avoid moving the stage, which would necessitate adjusting the focus of the light sheet midway through the time lapse acquisition.

scRNA-seq

Protoplasts were generated as follows: To collect roots enriched for different phases of the cell cycle, root tips were synchronized with 2mM HU media as described above. To process cells synchronized in different phases in parallel, seedlings were transferred to HU media in a staggered manner such that they would be ready for harvesting at the same time.

The distal-most 400 μm of approximately 500 root tips were excised from 7 DPG seedlings and then collected via capillary action with a P200 pipette tip containing 25 μL of protoplasting buffer. These root tips were then dispensed into cell wall degrading solution as previously described.[75] Root tips were gently agitated on an orbital shaker for approximately 1 hr and were gently pipetted up and down with a P1000 pipette every ten minutes after the first half hr of incubation. Root tips were then passed through a 40-micron cell strainer (product # 08-771-1, Fischer Scientific) and any large aggregates of cells were gently pressed against the strainer using sterile flat forceps to release any cells that had so far failed to dissociate.

10X libraries were prepared from protoplasts to generate scRNA-seq libraries using the Chromium Next GEM Single Cell 3′ Reagent Kit v3.1 (10X Genomics) following manufacturer's instructions.

The cDNA and sequencing library fragment sizes were both measured with the Agilent Tapestation 4200 using the high sensitivity 1000 (product # 5067-5582, 5067-5583) and 5000 (product # 5067-5592, 5067-5593) reagents respectively. Sample concentration was detected using the Qubit HS dsDNA (product # Q32851, Thermofischer) assay following manufacturer's instructions. Library quantitation for pooling was performed as follows: the fragment size and concentration of the library in ng/μL were used to determine the molarity of the libraries with the following equation: [Lib Conc (ng/μL)]/[(Frag Length (bp) * 607.4)+157.9] * 1000000. Libraries were then diluted to 3 nM concentration and pooled for sequencing. Samples were sequenced on a Novaseq 6000 using an SP flowcell in 28x91 paired end 100 cycle mode with V1.5 reagents (100 cycles).

Bulk RNA-seq

For bulk RNA-seq, total RNA was extracted from sorted protoplasts using the Qiagen RNA micro kit following manufacturer's instructions. RNA quality was determined using RNA high sensitivity reagents (product # 5067-5579, 5067-5580, 5067-5581, Agilent) for the Agilent TapeStation 4200. Total RNA was used to synthesize cDNA using the SMART-Seq v4 full-length transcriptome analysis kit from Takara (product # 634888) using protocol B specified in the manual on page 12. The quality of cDNA was then assessed using D1000 reagents for the Agilent Tapestation. The resulting cDNA was used to generate sequencing libraries with the Ovation Ultralow Library System V2 from Tecan (product # 0344) following manufacturer's instructions. Libraries were then sequenced on a Novaseq 6000 with an SP flowcell in 1x100 single end 100 cycle mode with V1.5 reagents (100 cycles).

Cells were collected by FACS as follows: Root protoplasts were sorted using a BD FACS Aria II using FACS Diva software.[76,77] Briefly, protoplasts were sorted directly from cell-wall degrading solution into a 1.5 mL microcentrifuge tube containing 350 μL of Qiagen RNA extraction buffer supplemented with beta mercaptoethanol.

Protoplasts expressing an H2B RFP fusion and a CDT1a GFP fusion under the native promoter were sorted and gated to remove doublets and debris. Then RFP positive events were identified by plotting red scale autofluorescence versus RFP and then gating for cells that showed RFP fluorescence above background as defined by a Col-0 control expressing no fluorescent proteins. In tandem, CDT1a positive cells were identified by plotting autofluorescence versus GFP and gated for GFP expression above background relative to Col-0 control. Then both the RFP+ and GFP+ populations were plotted in a histogram of RFP signal v. cell count. This identified a population with two RFP peaks characteristic of DNA staining in dividing cells. The GFP+ population (CDT1a reporter fluorescence) overlapped with the 2n ploidy peak, which is consistent with its expression in the G1 phase of the cell cycle and was used as a positive control. Further gates were defined based on the histogram to collect cells in G1 (2n), G2/M (4n), and S (intermediate RFP signal) phases. These populations were collected simultaneously in a three-way sort and the maximum number of cells were collected for each phase. This protocol was repeated independently twice to generate 6 samples for RNA-seq library preparation. Samples were snap frozen and stored at -80 degrees Celsius until all samples were collected and could be processed for RNA extraction and library preparation simultaneously.

In order to use cellular ploidy as a proxy for cell cycle phase, it was critical to harvest the distal-most portion of the root tip in order to avoid harvesting any cells that had already begun endoreduplication. The distal-most 200 μm of approximately 500 root tips were excised from 7 DPG seedlings and then collected via capillary action with a P200 pipette tip containing 25 μL of cell-wall degrading solution. These root tips were then dispensed into cell-wall degrading solution. Root tips were gently agitated on an orbital shaker for

approximately 1 hr and were gently pipetted up and down with a P1000 pipette every ten minutes after the first half hr of incubation. Root tips were then passed through a 40-micron cell strainer and any large aggregates of cells were gently pressed against the strainer using sterile flat forceps to release any cells that had so far failed to dissociate. The resulting protoplasts were then transferred to a test tube appropriate for the cell sorter and immediately processed via FACS.

Sequencing Data Analysis

Bulk RNA-seq

For Bulk RNA-seq, reads were trimmed using Trimmomatic version 0.39 in single end mode with the following settings: ILLUMINACLIP:TruSeq3-SE:2:30:10 LEADING:3 TRAILING:3 SLIDINGWINDOW:4:15 MINLEN:36. Trimmed reads were mapped to the Arabidopsis TAIR10 genome using HISAT2 version 2.2.1. Reads mapping to genes were counted with Rsubread (version 1.22.1) featureCounts in single end mode with a minimum overlap of 5 and counting only primary alignments and ignoring duplicates. Reads were normalized using the TPM calculation and the resulting count matrix was used to calculate mean values per condition, filtered to remove genes with low expression and low variance, and then clustered via k-means clustering. The number of k (8) was chosen to reflect the total permutations of expression changes (up or down) and cell cycle phases (G1, S, G2/M).

scRNA-seq

For scRNA-seq the mkfastq function in Cell Ranger 5.0.1 was used to generate fastq files from the raw sequencing output. Count matrices for scRNA-seq experiments were then generated with the count function and the TAIR 10.38 release of the Arabidopsis genome.

Quality Control – scRNA-seq

After generating count matrices using Cell Ranger, Seurat was used to filter cells based on the number of features detected (more than 2000 and less than 10000), percent mitochondrial reads (less than 5), and total RNA molecules detected (less than 100000). This produced datasets in which the R squared coefficient between features and counts exceeded 0.93, indicating that the remaining cells in the dataset were healthy singlets. Libraries were integrated using the sctransform workflow in Seurat.[78] To map cell identities onto cell cycle-annotated single cells, we used cell-identity markers identified in an independent analysis.[34]

Identifying Cell Cycle Markers

Cell type annotations were carried over from a control dataset that had previously been annotated based on the expression of cell type specific marker genes. Cell labels were carried over manually by examining the cluster membership of cells from the control library, which formed the same stable clusters as they had previously when integrated with this dataset. Previous cluster identity was then manually transferred to all cells from the HU-treated datasets that shared cluster membership with the annotated cells from the control dataset.

Transcriptional detection of phase enrichments for scRNA-seq libraries were validated by comparing upregulated genes in each scRNA-seq library with expression patterns in ploidy-sorted bulk RNA-seq. Due to the absence of a clear peak for S phase, we collected many fewer cells from S-phase. Thus, we did not expect a high overlap in this phase. However, phase agreements were high in both G2/M and G1 phases, validating the synchronization method. For S phase, upregulated genes in the enriched scRNA-seq libraries were enriched for functions already known to be core for S-phase including many histones. Thus, we used the scRNA-seq to generate markers because of its high resolution of each phase.

While the scRNA-seq libraries were enriched for cells in each phase of the cell cycle, their cell type composition was variable. To ensure the identification of cell cycle markers present in all cell types, we projected them on the same UMAP space, determined the lowest number of each cell type across all enriched libraries and then randomly down sampled each cell type in each library to produce libraries with equal cell type composition. We then performed differential expression analysis with cells from each phase enriched library using Seurat's FindAllMarkers function. Markers were ranked by percent differential expression and the top 50 for each library were chosen as cell cycle marker genes. Markers were then used to analyze the cell cycle in the full (not down sampled) scRNA-seq dataset and other non-synchronized scRNA-seq datasets.

In a separate analysis, we isolated individual cell types from the scRNA-seq dataset, grouped cells by phase and then performed a differential expression analysis to identify phase markers on a per cell basis. We filtered out genes with a p value great than 0.000001 and then constructed a cell type+phase by gene matrix, where each cell of the matrix contains a 1 if a gene is a marker for that cell type+phase combination, or a 0 if it is not a marker. That matrix is provided as Table S6.

Pseudotime Analysis

For cell cycle psuedotime analysis, Monocle3 was used to create the UMAP embeddings with the top 150 ranked genes for each phase of the cell cycle. We then used the learn_graph and order_cells functions to calculate a pseudotime trajectory for cells based on the cell cycle anchored in G2/M. To find genes that changed as a function of pseudotime we used the graph_test function. We then aggregated the gene expression matrix based on evenly spaced bins along the pseudotime trajectory and clustered those bins based on gene expression to assign genes to different positions in the pseudotime trajectory.

Data visualization was generated using ggplot2 with Tidyverse, Seurat, pHeatmap, Treemap and Monocle3.

Imaging Data Analysis

Long-term time-lapse images were registered in 3 dimensions by first detecting objects (either nuclei, WOX5, or WIP4 marker expression) and then using detected objects to correct the reference frame for the time lapse in 3 dimensions. The new reference frame was then used to correct the time lapse for both translational and rotational drift. Once drift corrected, nuclei were then segmented again

using the spot detection tool with the local contrast setting enabled to account for uneven background throughout the root or bleed through from other channels. Once segmented, statistics for all nuclei were exported to R for further analysis. Cell phase was determined by measuring the amount of YFP, CFP and mCherry signal in each nucleus. If CFP or YFP signal exceeded a detection threshold cutoff, cells were classified as G1 or G2M respectively. All other cells were classified as S phase. The PlaCCI reporter does not easily distinguish between cells in S phase versus early G2, so it is possible that some G2 cells were classified as S phase cells in this analysis. Counts of cells in G1 (Figure 3B), G1 durations (Figure 3D), and G1 exit time (Figures 3C and 6B) were determined manually. G1 duration time (Figure 3E) is normalized within each root to the duration of the time lapse. Survivorship curves are shown independently (pale lines) and as a LOESS regression of both replicates (dark lines). Some of the observed G1 events did not end during the time lapse in both the control (76 percent) and the ablation (38 percent) movies. In these cases, we measured G1 duration in three ways: 1) as the time between when CDT1a became visible and the final frame of the time lapse, 2) as equal to the observed G1 duration time for this region of the root, which is estimated to be longer than 20 hr,[7] and 3) as the fraction of total movie duration (Table S5). By all these metrics, the difference in G1 duration is statistically significant (Mann-Whitney test, p-value = 1.614e-08, p-value = 2.04e-05, or p-value = 3.221e-09). The log rank test was used to determine the significance of the G1 survivorship analysis.[79]

For still images, 3-dimensional segmentation was performed in TrackMate by treating the Z dimension as a time dimension. Nuclei were segmented based on the HTR13-mCherry channel and then data for each channel within nuclei was exported to R for further analysis. In the case where a single slice was taken, all nuclei were similarly segmented in TrackMate in one dimension and retained.

Confocal image stacks were taken such that nuclei would appear in at least two consecutive slices. Therefore, all nuclei that appeared in only one slice were discarded. For the remaining nuclei, or for all nuclei in the case of images acquired as median slices, Blue CMAC signal was scaled from 0 to 1 per cell file to render nuclei comparable. In the case of short-term time lapses of PlaCCI roots stained with Blue CMAC taken using confocal microscopy, drift was corrected in 2 dimensions using the Correct 3D drift plugin in FIJI prior to Trackmate segmentation. Nuclei were filtered if they were not tracked for the entire time lapse. Blue CMAC signal was calculated as a change over the value at time zero. Tissues were classified into specific identities for quantification of GSH content using relative cell position and root morphology.

In Situ Hybridization

Candidate probes were selected from the top marker set described above if they were expressed in at least 80 percent of cells from the target phase and if they exceeded a differential expression threshold of 0.25 LFC based on a differential expression test performed in Seurat. Then the average expression for each gene in the marker set within a given phase was calculated. The top 5 most highly expressed genes from each phase that had passed the differential expression filtering step were chosen as candidates for further analysis. The expression of this small set of genes was examined manually to ensure there was no cell-type-specific bias. Finally, the most strongly expressed candidates from this set were chosen for probe design. Genes from these sets that had either unknown function or were not previously characterized as being cell cycle controlled were prioritized. Probe design was performed by Molecular Instruments. Sample preparation for *in situ* hybridization was performed as described previously for monocot roots[80] with the minor modifications. Briefly, roots were fixed in a paraformaldehyde (4%), glacial acetic acid (5%), ethanol (50%) buffer and then dehydrated with a series of ethanol washes (50% - 100%), rinsed twice with 100% methanol and then held in 100% methanol overnight. The next day methanol was removed from samples with ethanol washes and then samples were permeabilized via incubation in 50% ethanol/50% Histo-Clear (Electron Microscopy Sciences #64110). Samples were then incubated in 4% paraformaldehyde in DPBS-T after which hybridization was performed following manufacturer's instructions provided by Molecular Instruments.

QUANTIFICATION AND STATISTICAL ANALYSIS

For scRNA-seq statistical analysis, differential expression tests to identify markers were performed using Seurat in R and the results of that statistical test are reported in Table S1. For imaging and regeneration data, statistical tests are reported throughout the manuscript and are available in figure legends. All statistical tests were performed in R. Statistical tests for data comprised of count variables were performed using the Wilcoxon test implemented in the rstatix package. Where noted, count data was tested using the Chi-square test with the stats package. Statistical tests of data comprised of continuous variables was performed with rstatix using the pairwise t-test function. The log rank test was used to determine the significance of the G1 survivorship analysis.[79,81] Loess regressions are shown throughout the manuscript with 95% confidence intervals calculated by the ggplot2 smooth function. Wherever n is less than 30, results are plotted as a combined box and jitter plot so that the n number is visible in the summary plot. Where n is greater than 30, the *n* value is annotated onto the summary plot.

Where fluorescence results are quantified, they are represented as the corrected total cellular fluorescence (CTCF) where the area of the relevant ROI was multiplied by the average fluorescence intensity of the background signal of the image. This value was then subtracted from the integrated density value of the ROI. Each of these values was obtained in FIJI using the measure function. ROIs were either determined manually based on the expression domain of a reporter gene, or were determined with automatic

segmentation for all visible nuclei using either TrackMate or Imaris. In the case of *in situ* imaging experiments, ROIs were determined by manually segmenting cells based on the DAPI counterstain channel. Images were then thresholded to remove background, and the corrected total cell fluorescence (CTCF) was calculated within each ROI as described above. Cut offs to separate cells with signal from background were determined using change point analysis.[82] Permutation and bootstrap tests to determine the p-value and the confidence interval of the anti-correlation were performed in R.

Gene ontology enrichments were determined using the gene list analysis portal in Thalemine.

Developmental Cell, Volume *60*

Supplemental information

Glutathione accelerates the cell cycle and cellular reprogramming in plant regeneration

Laura R. Lee, Bruno Guillotin, Ramin Rahni, Chanel Hutchison, Bénédicte Desvoyes, Crisanto Gutierrez, and Kenneth D. Birnbaum

Supplemental Figures

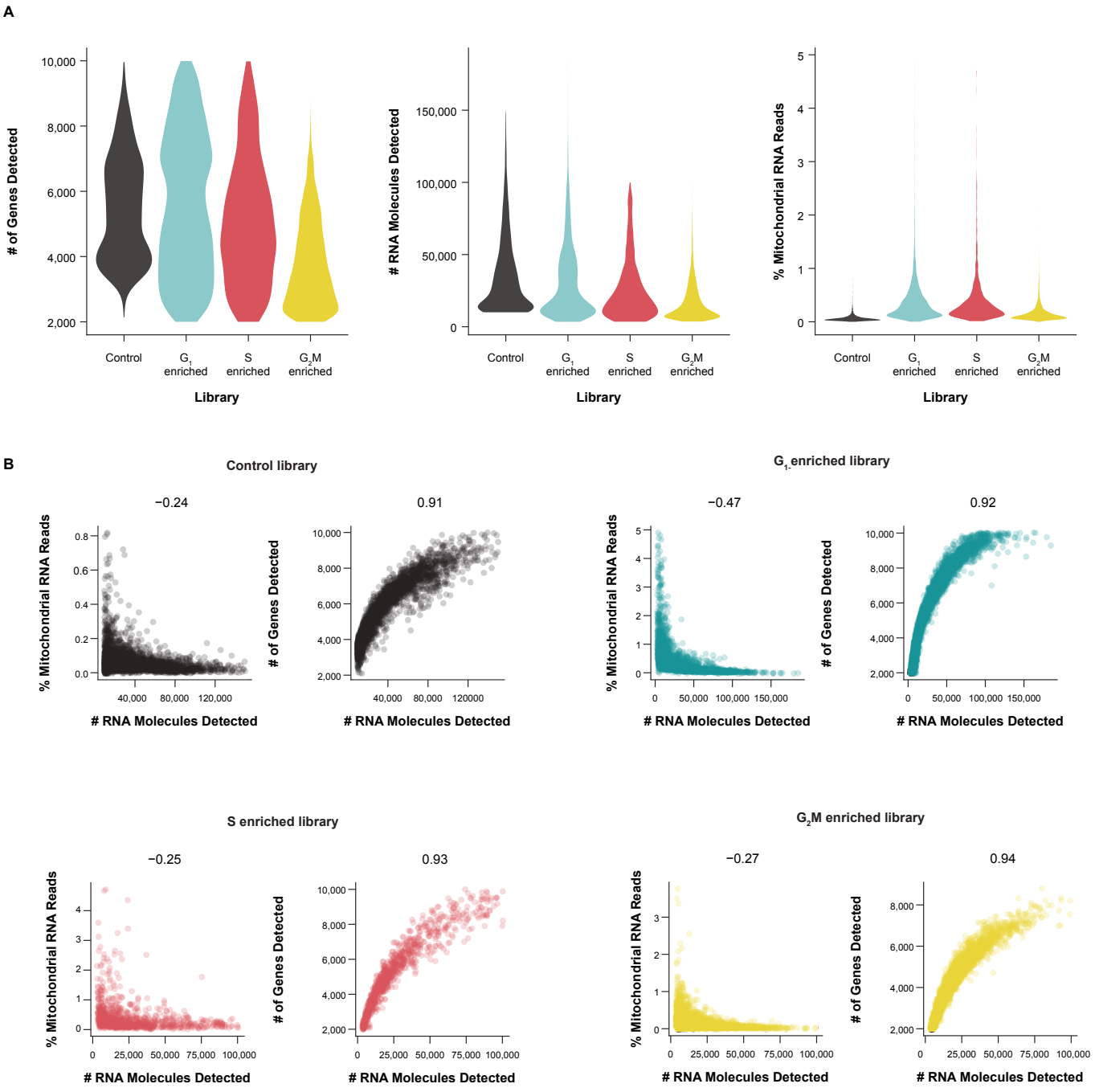

<u>Figure S1</u>. Single Cell RNA-seq profiles show robust signals in quality control; Related to Figure 1. (A) Violin plots showing the number of genes, RNA molecules, and the percentage of reads from mitochondrial genes, per cell in each scRNA-seq library. (B) For each library, a pair of scatter plots shows (1) the anti-correlation between percent mitochondrial reads and number of RNA molecules detected (at left), and (2) the correlation between the number of genes and the number of unique RNA molecules detected (at right). Correlation coefficient is shown above the plot.

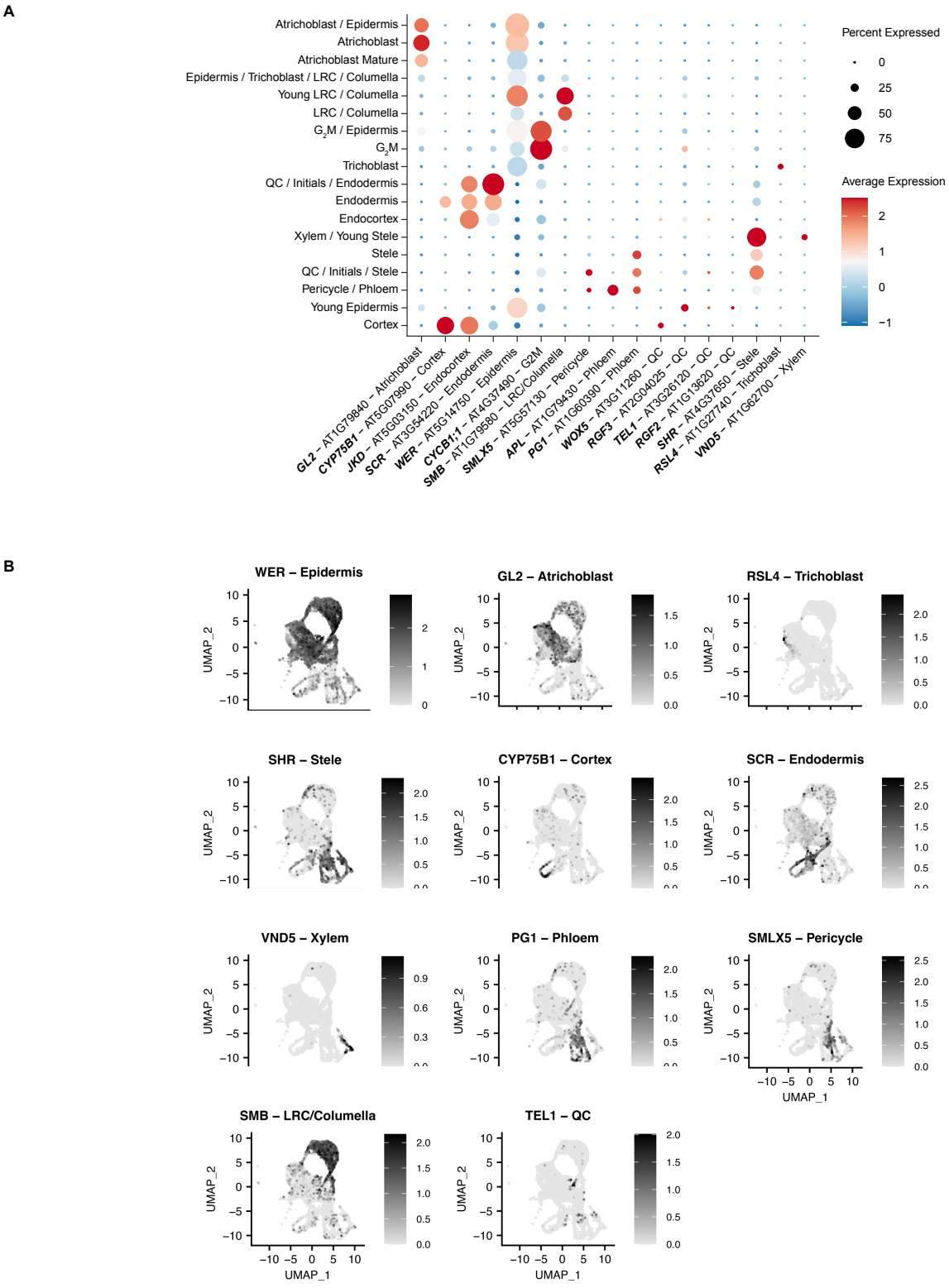

Figure S2: Markers robustly identify cell types in phase-enriched libraries; Related to Figure 1. (A) A dot plot showing the expression of marker genes across clusters defined by cell type in the integrated phase-enriched libraries. Size of the dot shows the percentage of cells in a cluster expressing the marker and the colormap shows the average expression of the marker in the cluster. (B) UMAPs highlighting the highly localized expression of various cell type-specific marker genes, as expected for robust capture of cell identities in scRNA-seq profiles. The cells are not grouped by phase and the ability to capture clusters with clear cell identity demonstrates the overall quality of the cells.

A

	G_1 enriched	S enriched	G_2M enriched
Atrichoblast	74	74	74
Atrichoblast / Epidermis	15	15	15
Atrichoblast Mature	20	20	20
Cortex	12	12	12
Endocortex	14	14	14
Endodermis	3	3	3
Epidermis / Trichoblast / LRC / Columella	89	89	89
G_2M	128	37	554
G_2M / Epidermis	8	8	8
LRC / Columella	186	186	186
Pericycle / Phloem	28	28	28
QC / Initials / Endodermis	18	18	18
QC / Initials / Stele	115	115	115
Stele	23	23	23
Trichoblast	45	45	45
Xylem / Young Stele	36	36	36
Young LRC / Columella	169	169	169
Young Epidermis	112	112	112

B

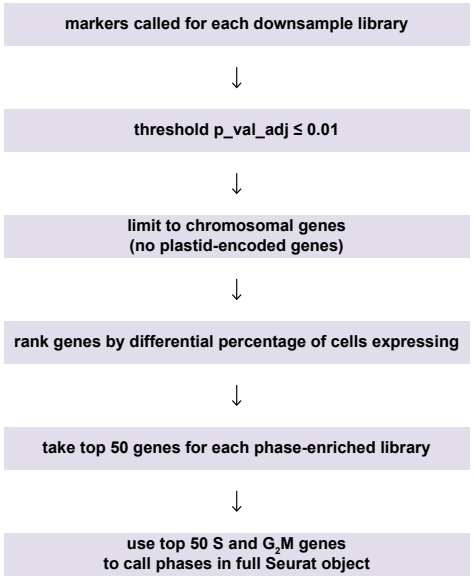

C

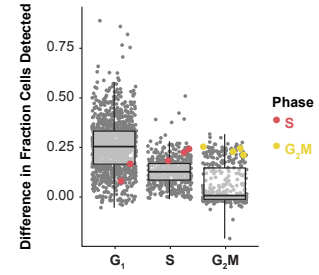

D

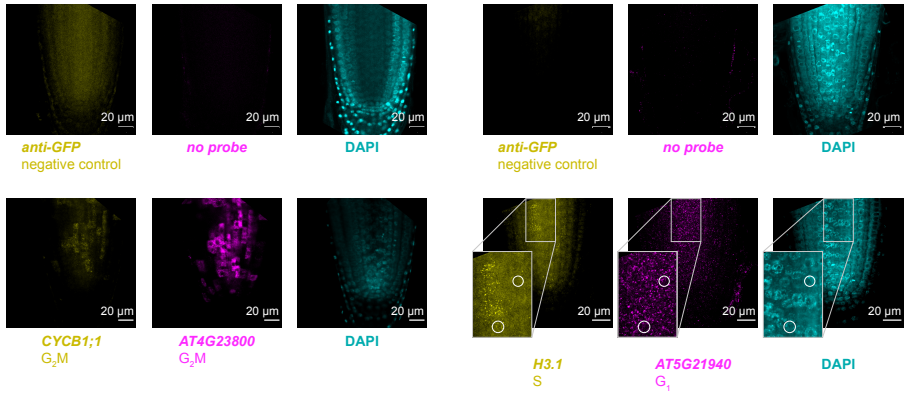

E

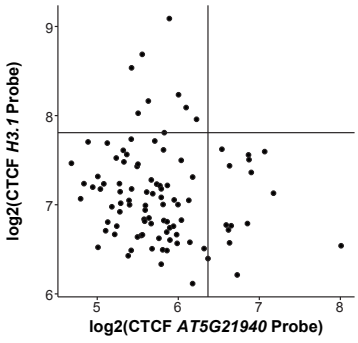

F

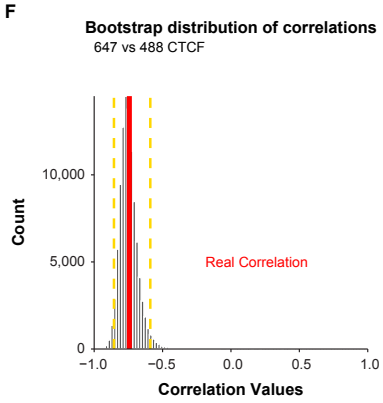

G

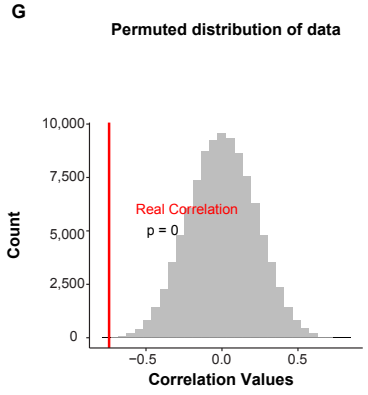

<u>Figure S3</u>. Data analysis methods identify cell phase markers with *in situ* validation of a new G1 marker; Related to Figure 1. (A) Cell counts for down-sampled phase-enriched libraries, ensuring each cell type contributed an equal number of cells to each phase enrichment analysis and every cell type is accounted for in the phase enrichment analysis. (B) Differential expression analysis pipeline to identify phase markers. (C) Genes (each dot) categorized as differentially expressed in specific phase-synchronized libraries. The y axis represents the difference in the fraction of cells in which the gene is expressed in target versus non-target libraries. The highlighted genes are gold standard markers of phase-specific expression, showing high expression in many cells in the appropriate phase-synchronized library (x axis categories). (D) Representative

images of G2M (left) and S phase (right) markers from *in situ* hybridization experiments shown with their corresponding negative controls as annotated. Insets highlight examples of cells where G1 and S probe signal is anti-correlated, which is quantified in E. (E) Anti-correlation with signal cutoffs shown for H3.1 (S phase) and AT5G21940 (G1) probes with signal cutoffs determined empirically via change point analysis[83]. Values come from three root median sections in which all cells were hand segmented based on DAPI counterstain. (F) Bootstrap distribution of correlation values between H3.1 and AT5G21940 probe signals shows the determined anti-correlation falls within the 95% confidence interval (yellow dotted lines). (G) Permutation distribution of the correlation between H3.1 and AT5G21940 probe signals shows the actual anti-correlation falls well outside of the null distribution (p-value = 0).

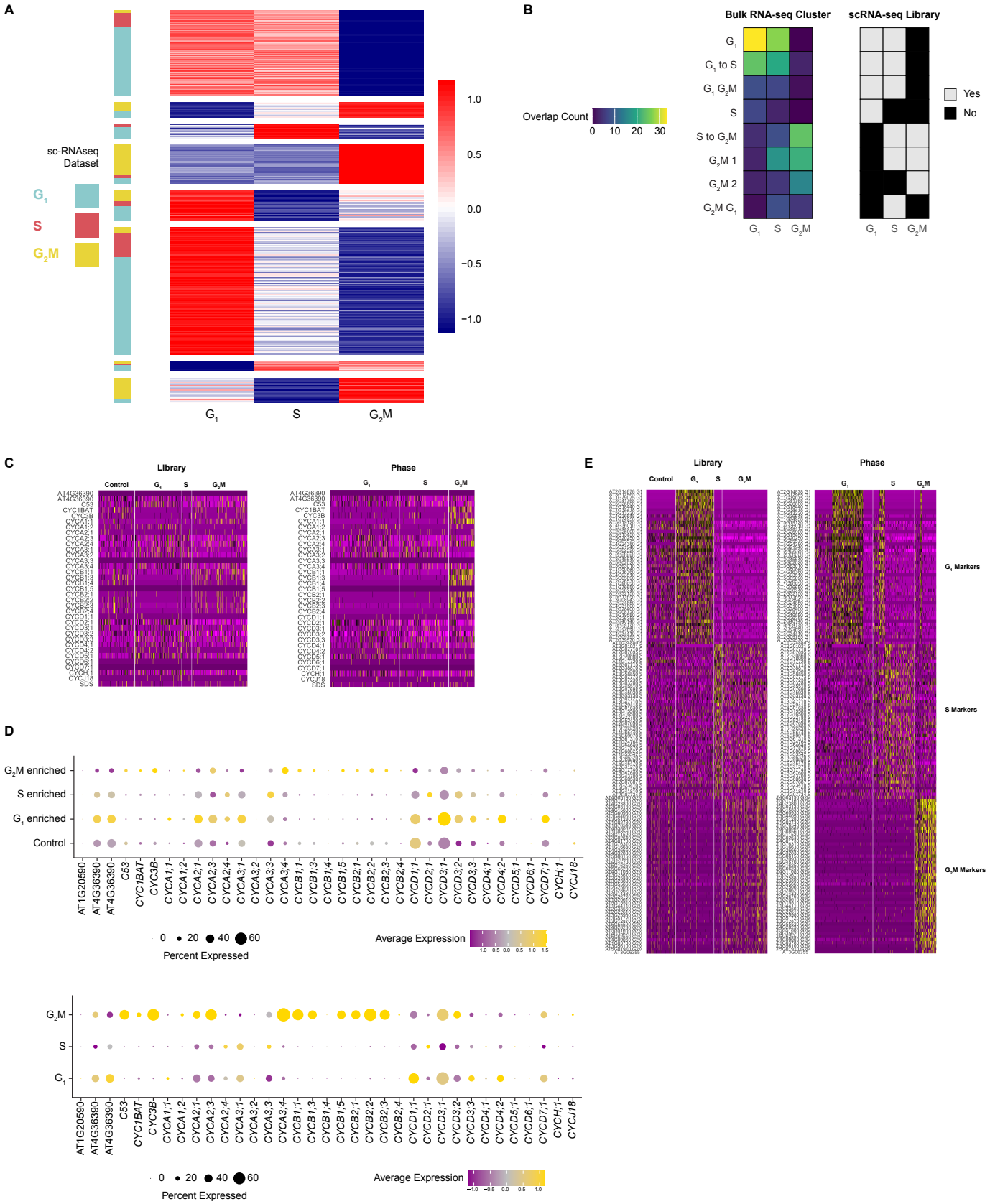
A
sc-RNAseq Dataset
G1
S
G2M
1.0
0.5
0.0
−0.5
−1.0
G1
S
G2M
B
Overlap Count
0 10 20 30
Bulk RNA-seq Cluster
scRNA-seq Library
G1
G1 to S
G1 G2M
S
S to G2M
G2M 1
G2M 2
G2M G1
Yes
No
C
Library
Phase
Control
E
G1 Markers
S Markers
G2M Markers
D
G2M enriched
S enriched
G1 enriched
Control
AT1G20590
AT4G36390
AT4G36390
C53
CYC1BAT
CYC3B
CYCA1;1
CYCA1;2
CYCA2;1
CYCA2;3
CYCA2;4
CYCA3;1
CYCA3;2
CYCA3;3
CYCA3;4
CYCB1;1
CYCB1;3
CYCB1;4
CYCB1;5
CYCB2;1
CYCB2;2
CYCB2;3
CYCB2;4
CYCD1;1
CYCD2;1
CYCD3;1
CYCD3;2
CYCD3;3
CYCD4;1
CYCD4;2
CYCD5;1
CYCD6;1
CYCD7;1
CYCH;1
CYCJ18
0 20 40 60
Percent Expressed
Average Expression

Figure S4: Bulk RNA-seq profiles and classic cell cycle markers confirm phase-enriched scRNA-seq libraries; Related to Figure 1.

(A) Gene expression heatmap (red and blue) in which each row is a gene and each column represents the average expression profile across bulk RNA-seq profiles where the three libraries represent cells sorted by ploidy level as a proxy for phase. The color bar to the left indicates the independent cell cycle phase classification of each gene from analysis of the synchronized scRNA-seq library. In the bulk RNA-seq analysis, genes were grouped into 8 k-means clusters. Agreement between the two independent analyses is indicated by groups of genes showing a scRNA-seq classification and enrichment in the appropriate ploidy-sorted cell library. Strong agreement is shown for G1 and G2/M, while S-phase is not well defined in the ploidy sorting. (B) Heatmaps showing the number of overlapping genes (left) and the statistical significance of the overlap (right) between differentially expressed genes from phase-enriched scRNA-seq libraries (columns) and gene expression clusters of ploidy-sorted cells determined by k-means clustering (rows). 'Yes' = statistically significant overlap at $p<0.05$ by Fisher's exact test. See also Table S1. C) Heatmaps comparing expression of classical cell cycle markers (rows) in cells (columns) grouped by the phase enrichment library from which they came (left), which may still contain cells from a mixture of phases, vs. cells assigned to phase based on markers determined by our analysis pipeline (right). At left, some enrichment of markers is visible but phase-enriched libraries still contain cells in the non-target phase. At right, enrichment of known markers is more prominent when cells are assigned to phase by our analysis pipeline, which is independent of the expression of the classical cell cycle markers. (D) A summary analysis of the heatmap data in C. Dotplots show the expression of cyclins in phase-enriched libraries (top) vs phases assigned with our top marker genes (bottom). Cyclins are expressed in the appropriate datasets despite their sparseness (top). For example, CYCDs show the highest average expression in the G1-enriched library and CYCBs show the highest average expression in the G2/M-enriched library. Cyclin expression behaves well based on phase assignments performed with our marker genes (bottom). (E) Following the same comparison as in C with the top 50 markers assigned by our pipeline. At left, the markers are shown based on their enrichments in the different phase libraries. These agree with classical markers but the analysis shows the new markers have higher expression and are more frequently detected in single-cell profiles. At right, the analysis shows cells classified by phase using the top 50 markers. Overall, the analysis showed that markers for G1 and S phases had expression patterns that were enriched in but not strictly exclusive to their respective phase. For example, S-phase markers, while most highly expressed in that phase, often had low levels of expression in G1 and vice versa. While G2/M was transcriptionally distinct, G1 and S had more continuous expression patterns. However, the full set of markers for each phase, including G1, robustly assigned root cells to a specific phase in scRNA-seq datasets.

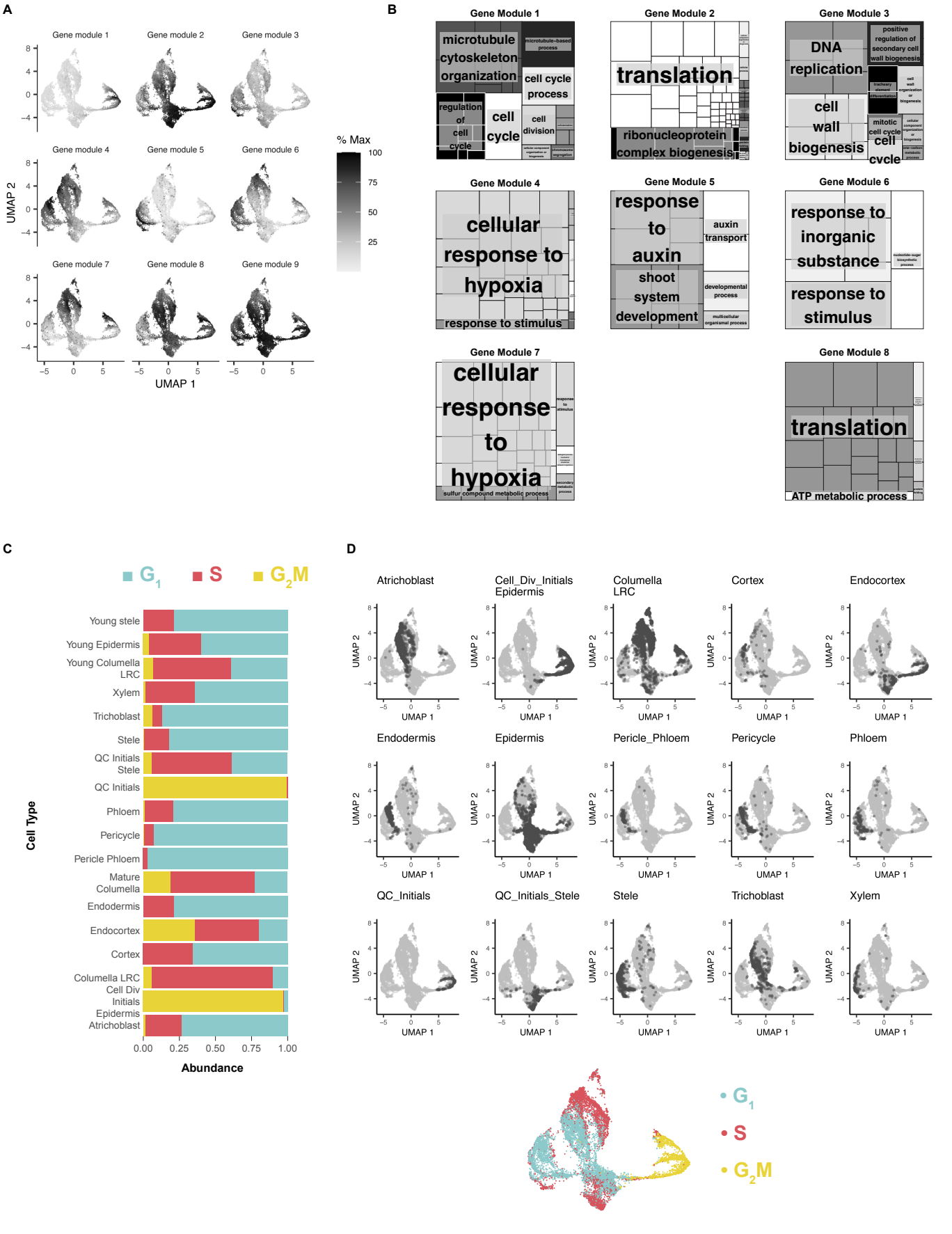
A
Gene module 1
Gene module 2
Gene module 3
Gene module 4
Gene module 5
Gene module 6
Gene module 7
Gene module 8
Gene module 9
UMAP 2
UMAP 1
% Max
100
75
50
25
B
Gene Module 1
microtubule cytoskeleton organization
microtubule-based process
cell cycle process
regulation of cell cycle
cell cycle
cell division
Gene Module 2
translation
ribonucleoprotein complex biogenesis
Gene Module 3
DNA replication
positive regulation of secondary cell wall biogenesis
cell wall biogenesis
mitotic cell cycle
cell cycle
Gene Module 4
cellular response to hypoxia
response to stimulus
Gene Module 5
response to auxin
auxin transport
shoot system development
developmental process
Gene Module 6
response to inorganic substance
response to stimulus
Gene Module 7
cellular response to hypoxia
sulfur compound metabolic process
Gene Module 8
translation
ATP metabolic process
C
G1
S
G2M
Young stele
Young Epidermis
Young Columella LRC
Xylem
Trichoblast
Stele
QC Initials Stele
QC Initials
Phloem
Pericycle
Pericle Phloem
Mature Columella
Endodermis
Endocortex
Cortex
Columella LRC
Cell Div Initials
Epidermis
Atrichoblast
Cell Type
0.00
0.25
0.50
0.75
1.00
Abundance
D
Atrichoblast
Cell_Div_Initials Epidermis
Columella LRC
Cortex
Endocortex
Endodermis
Epidermis
Pericle_Phloem
Pericycle
Phloem
QC_Initials
QC_Initials_Stele
Stele
Trichoblast
Xylem
UMAP 1
UMAP 2
G1
S
G2M

Figure S5. Cells of the same identity group together even when clustered by only cell cycle markers; Related to Figure 2. (A) Analysis of gene modules that are preferentially expressed along the cell cycle pseudotime ordering, as determined by Monocle3 (see Methods). Grayscale shows the aggregate gene expression of each gene module. (B) GO-terms associated with the corresponding gene module shown in A. No significant GO terms were found for gene module 8. (C) Relative abundances of phases among each cell type are shown. (D) UMAP outputs of pseudotime analysis clustered using the top 50 cell cycle markers with an independent analysis of cell identity mapped onto the UMAP trajectories. In each panel, a different cell type is highlighted in dark grey. Below, a key shows the cell cycle classification for each cluster in the UMAP.

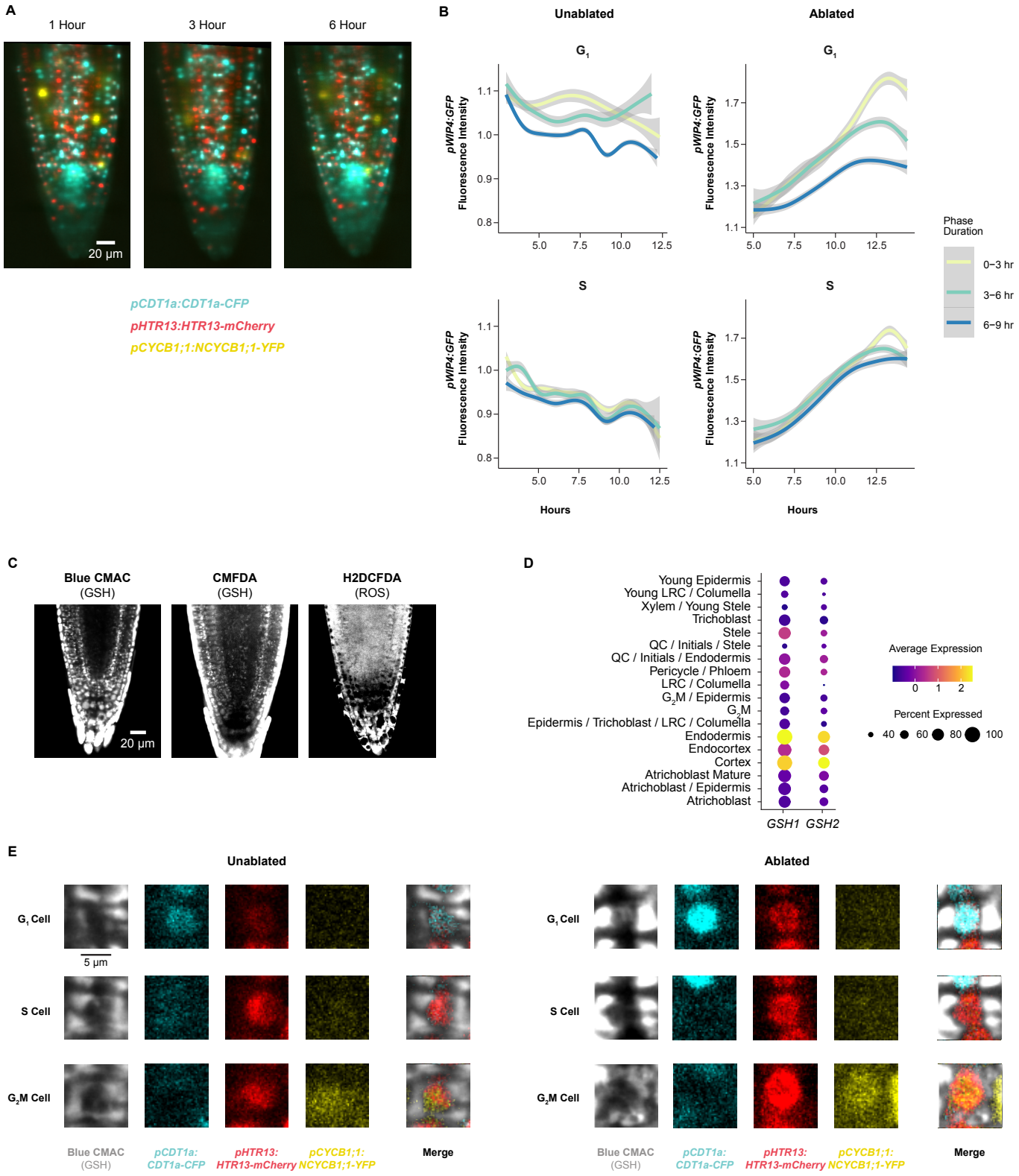

Figure S6: The appearance of newly reprogrammed cell identity correlates with rapid G1 phases caused by high nuclear GSH; Related to Figures 3 and 4. (A) Representative images of a control root expressing PlaCCI and *pWIP4:GFP* at 1, 3, and 6 hour time points during a time-lapse acquisition, showing consistent distribution of each of the three markers over time under imaging conditions in unablated roots. (B) Quantification of the *pWIP4:GFP* signal intensity in G1 phase and S phase cells over the duration of time-lapse movies in unablated roots. The figure represents the complete analysis of data shown in primary Figure 3E. (C)

Representative confocal microscopy images of seedlings stained for GSH (Blue CMAC, CMFDA) or ROS (H2DCFDA) under control conditions. Note that the two GSH dyes agree and show prominent ground tissue staining. Note that CMFDA and H2DCFDA, with similar chemical structure but different target molecules, show different staining patterns. (D) Expression of *GSH1* and *GSH2* represented as a dot plot derived from scRNA-seq profiles in different root cell types. Note the prominent expression in endodermis and cortex, in agreement with the GSH dyes. (E) PlaCCI signal for cells shown in Figure 4D, in order to show the cell cycle phase in frame one of the time lapse, 00:00 (hh:mm). There is a low but detectable enrichment of Blue CMAC signal in the G1 nucleus at this time point prior to ablation. Exogenous application of GSH did not cause a shift in the number of G1 cells (root n = 37, nuclei n = 9100, no significant difference between treatment and control by student's t-test).

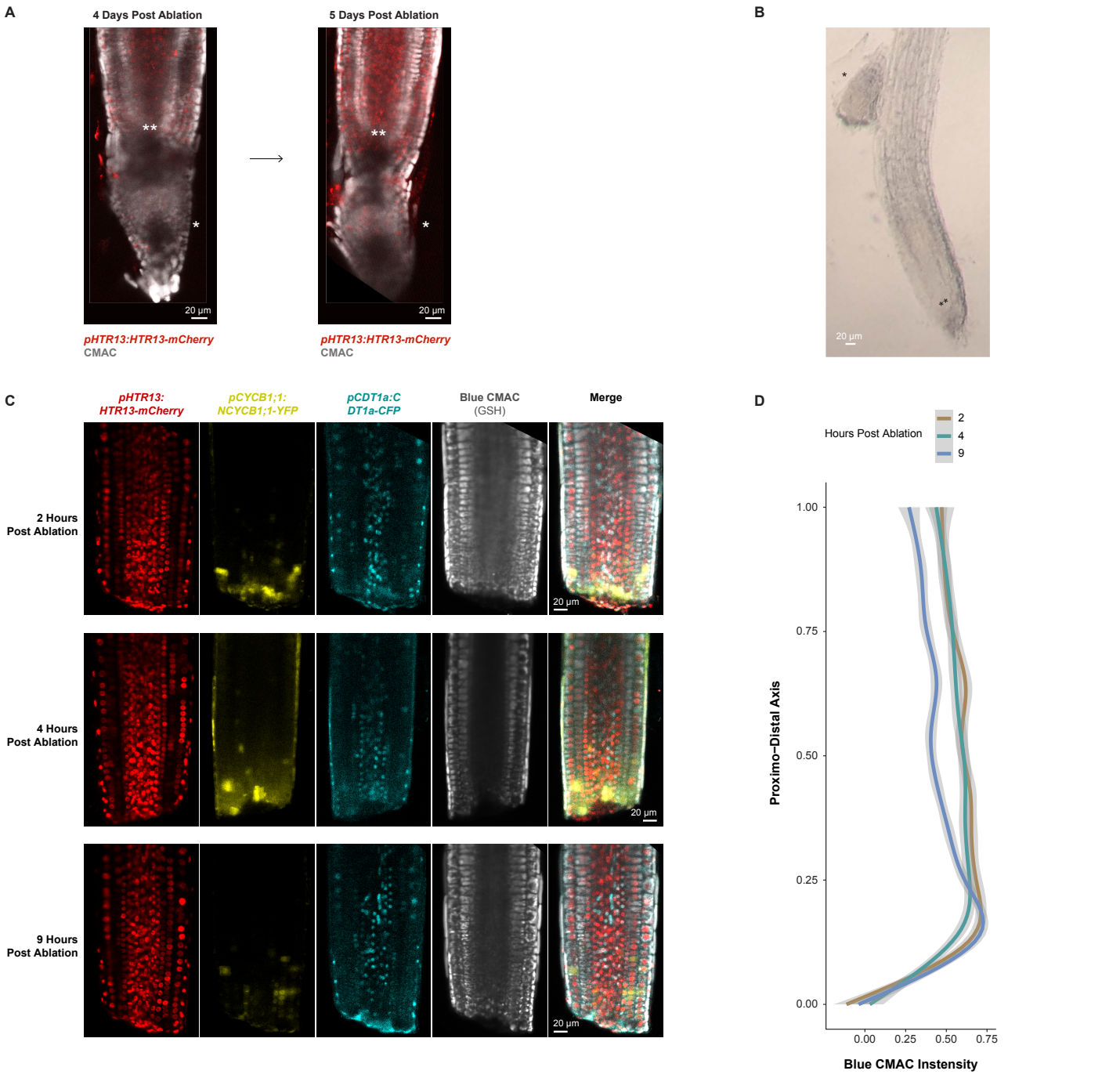

<u>Figure S7</u>. New meristem formation and GSH nuclear localization dynamics during regeneration; Related to Figure 4. (A) Representative confocal images of roots of seedlings grown on standard ½ MS and then mounted in an imaging cuvette undergoing regeneration. Between days 4 and 5 post ablation it becomes apparent that new columella above the ablation is established proximal (shootward) to the original QC (*), which is below the ablation. The new tapered root cap, which includes the columella, is apparent distal to the new QC (**), both of which are above the ablation site. (B) At a later time point, the original root tip (*) is sloughed off as growth continues from the new QC/stem cell niche (**) in the same seedling shown in A. The image is unscaled but the scale bar is estimated to be ~20 microns based on maximum root width. (C) Representative confocal images of PlaCCI roots stained with Blue CMAC. Images were taken 2, 4, and 9 hpc. (D) Quantification of nuclear CMAC staining intensity along the proximo-distal axis at different time points after ablation. The y-intercept represents the ablation site, and the range of the y-axis represents the visible length of root imaged in the frame as shown in C. Note the peak of CMAC intensity right above the cut site between

0.00 and 0.25 on the longitudinal axis of the root (y-axis), which is highest at 2-4 hours post cut and begins to dissipate above point 0.25 at 9 hours.

Supplemental Tables

Table S2. Gold standard markers from prior transcriptional studies; Related to Figure 1.

Gene ID	Gene Name	Phase
AT3G27360	HTR3	S
AT5G10390	HTR13	S
AT2G28740	H4	S
AT4G14700	ORC1a	S
AT4G12620	ORC1b	S
AT2G37560	ORC2	S
AT5G16690	ORC3	S
AT2G01120	ORC4	S
AT4G29910	ORC5	S
AT1G26840	ORC6	S
AT2G29680	CDC6a	S
AT1G07270	CDC6b	S
AT3G54710	CDT1b	S
AT2G31270	CDT1a	S
AT1G44900	MCM2	S
AT2G16440	MCM4	S
AT5G46280	MCM3	S
AT2G07690	MCM5	S
AT5G44635	MCM6	S
AT4G02060	MCM7	S
AT5G43080	CYCA3;1	S
AT1G47210	CYCA3;2	S
AT1G08560	KNOLLE	G2
AT4G37490	CYCB1;1	G2
AT5G06150	CYCB1;2	G2
AT2G26760	CYCB1;4	G2

Table S5. G1 duration summary; Related to Figure 3.

Condition	Replicate	Movie Duration	G1 end observed?	Median G1 Duration (h)	Number of events	Median G1 Duration by condition (h)	Median max G1 Duration by condition (h)	Median Duration Fraction (h in G1/total movie length)
Ablation	1	12	No	7.33	17	3.7	3.7	0.3
			Yes	1.83	25			
	2	12.8	No	5.17	6	3.3	3.3	0.3
			Yes	2	12			
Control	1	13.3	No	10.2	15	11.5	20	0.9
			Yes	6	7			
	2	8.3	No	6.83	11	6.83	20	0.8
			Yes	6.33	1			